

TREBALL FINAL DEL GRAU EN ENGINYERIA FÍSICA

INVESTIGATION OF
CATHODOLUMINESCENCE
EMISSION FROM SI AND AU/SI
NANOSTRUCTURES

Author: Yago Nel Vila Gracia

Co-directors: Anatoly Zayats, Jordi Llorca Piqué

London, June 2017

Table of Contents

1. Abstract.....	2
2. Introduction.....	3
3. Fundamentals.....	5
3.1. Theory of Plasmonic excitations.....	5
3.2. Cathodoluminescence.....	9
3.3. Cathodoluminescence Spectroscopy setup.....	11
3.4. Optical Spectroscopy setup.....	15
3.5. Fabrication methods.....	17
3.6. COMSOL Multiphysics modeling.....	20
4. Results and Discussion.....	22
4.1. Silicon nanostructures.....	23
4.1.1. “Isolated” Nanorods.....	24
4.1.2. “Isolated” Nanopillars.....	30
4.1.3. “Non-Isolated” Nanopillars.....	33
4.2. Gold/Silicon nanostructures.....	35
4.2.1. “Isolated” Nanorods.....	36
4.2.2. “Isolated” Nanopillars.....	42
4.2.3. “Non-Isolated” Nanopillars.....	45
5. Conclusions and perspectives.....	49
6. Acknowledgements and conference papers.....	51
7. Bibliography.....	52
Annex I: Explanation of asymmetric excitations in Au/Si nanorods.....	i

1. Abstract

It has been many years that plasmonic resonances are studied to confine and direct light in the nanoscale. Recently, this progress in the nanophononics field has increased considerably driven mostly by the ability that optically resonant nanostructures present to enhance near-field effects controlling far-field scattering. The basis of this phenomenon relies in the surface plasmon polaritons (SPPs), which are electromagnetic surface waves that propagate at metal-dielectric or metal-air interface once the sample is properly excited. Thus, a complete investigation and comprehension of the plasmonic excitation behaviors that can arise for different materials and geometries has become essential to further innovate and improve the nowadays technology and life quality, together offering an alternative way with a different basis than the conventional electronics. Some of the photonic leading areas are the sensing and bio-sensing, solar cells, information storage and thermotherapy.

Moreover, another nanophotonic branch has gained popularity in the last few years. The study of optical resonances in dielectric materials that possess a high refractive index is gaining attention owing to we can induce, using suitable parameters such as size, grating, and type of material, both electric and magnetic resonances accounting the same order of magnitude with quite low dissipative losses.

During this project, a sample containing silicon (Si) nanostructures (nanorods and nanopillars) in a Si substrate is analyzed to study its optical properties and resonances. Afterwards, the Si sample is recovered by a gold (Au) layer, which will enable us to study both plasmonic and optical resonances. Through all the project, the main technique used is Cathodoluminescence (CL) spectroscopy. Moreover, we have proposed a model in COMSOL Multiphysics to simulate the resonance peak behaviors in the Visible range and we have performed some Optical spectroscopy measurements to give further insight in the comprehension of the nanostructure resonances.

2. Introduction

The late 20th and early 21st centuries have witnessed not only the invention but the large-production adoption of many technologies related to communication and computation. Thus, we can talk nowadays about transistors and diodes, and therefore, phones and computers.

It is the increasing dependence that the society manifests to the technology what impulses it to be faster, more efficient and cheaper. Accordingly to Moore's Law, the number of transistors is roughly duplicated every two years [1], so one can expect that the computation power increases accordingly. Logically, referring to electronic devices this rhythm of growth is not expected to last much longer because there are limiting factors that become relevant at small scales such as quantum mechanical effects, resistive-capacitance delays and power consumption magnification [2].

Thus, Nanotechnology and, particularly, Photonics field aim to take the lead in the new technology era regarding that photonic devices are based on the transmission of light and not electrons, coping with the electronic problems and rendering faster transmission rates. Moreover, both optical and plasmonic resonances can arise in the same range of wavelengths allowing the manipulation of light at the nanoscale and opening a wide window of possibilities and applications in fields such as sensing and bio-sensing [3], thermotherapy, solar cells [4] and information storage [5].

To continue improving and developing new devices that satisfy the evolving society necessities, we first need to fully comprehend the nature and behaviors regarding the nanostructures and metamaterials, which conform the key components of the plasmonic devices, and its resonant modes and wavelengths for different geometries, sizes and materials (dielectrics and plasmonics). This knowledge is essential to, therefore, create devices able to enhance and transmit light at the nanoscale.

The ability that optically resonant nanostructures present to enhance near field effects controlling far field scattering through interferences is one of the main reasons that explain the rapid progress that nanophotonics field is experiencing currently. These effects are mostly achieved by metamaterials, materials crafted synthetically standing nanostructures accounting different geometries, sizes, gratings and material

compositions. Habitually, plasmonic nanostructures such as gold (Au) have been the most used in the photonic devices to enhance and direct light at the nanoscale.

During the last decades, silicon (Si) has been the element most used in all electronic devices such as transistors and computer chips due to its abundance, which makes it cheap, and because it is a semiconductor with high tunability. But only in the last years, Si has attracted an important interest in the Photonics field as a high refractive index dielectric material with very promising properties such as the manipulation of the strong optically induced electric and magnetic Mie-type resonances, which makes it suitable to complement or even substitute, for some applications, the plasmonic metal materials [6]. Among others, dielectric nanostructures can find Photonics novel applications in integrated optical components, microcavity lasers [7] and light scattering layers in photovoltaics [8].

In this project, we study several optical and plasmonic resonance behaviors and their nature by means of a metamaterial sample made of a Si substrate and standing Si nanostructures (nanorods and nanopillars) with ranging sizes from 150 to 550 nm. The main technique used is the Cathodoluminescence (CL) Spectroscopy, which will allow us to obtain resonant CL Intensity maps and CL Intensity spectra in the visible range of wavelengths.

In the second part of the project, the Si sample is completely recovered with an Au 35 nm-thick layer. Thus, we can study and analyze both optical and plasmonic resonances arising in the visible range regarding different geometries and sizes. Moreover, we will also realize measurements in the Visible spectroscopy to distinguish and to give a broader insight accounting the nature of the arising resonances in the array. Finally, we have proposed a model in COMSOL Multiphysics to simulate the resonance behaviors for Si and Au/Si nanorods and to contrast them with the experimental CL intensity spectra obtained by means of CL spectroscopy.

This project aims to broaden the knowledge in the nanophotonics field by presenting and discussing different resonances and modes encountered among the plasmonic and dielectric nanostructures with different geometries, sizes and gratings.

3. Fundamentals

3.1. Theory of Plasmonic excitations

There are a multitude of processes that occur when an electron beam (about 30 keV) hits a sample and they depend, in turn, in the material's composition, its geometry and the surrounding system. The first event that occurs when the electrons interact with matter is the generation of low-energy secondary electrons (SEs) as ionization products. Afterwards, more energetic backscattered electrons are emitted (BSEs). Both emissions are wide used in microscopy.

Moreover, a high energy electron beam generates a broad spectrum of electromagnetic radiation in the sample ranging from x-rays to the mid-IR through a variety of coherent and incoherent processes. The radiation that accounts wavelengths within the visible and near-IR (NIR) ranges is known as Cathodoluminescence (CL); name given owing to the radiation is generated by cathode rays (fast electrons).

The coherent radiation, so-called because of the fixed phase relation between the incident electric field and the emitted radiation, englobes transition radiation (TR), surface plasmon polaritons (SPPs) and Cherenkov radiation.

As a matter of fact, TR and SPPs conform the dominant radiation in metals when they are excited, owing to fast non-radiative recombination of free electrons. On the other hand, incoherent radiation such as luminescence generated by band-edge electron-hole recombination is much stronger in semiconductors and thus, it does not usually interfere to coherent radiation [9].

It is known that an electron moving at a constant velocity carries evanescent electromagnetic fields that propagate away from the electron without the ability to couple to propagating radiation [10]. Though, when there is an electron-matter interaction, these evanescent fields can be coherently transferred and converted to free-space radiation. In this context we find the TR (Figure 1b), it arises when the electrons travel through two media with different refractive indices, consequently inducing a vertical dipole moment that can radiate in the far-field accounting a doughnut

emission, a broad spectrum highly space-localized and thus, a broad distribution in available momenta [11].

In relation to SPPs, they are essentially light waves trapped that propagate on a metal's surface owing an excitation of the free electrons present in a conductor (observed in Figure 1a). The coupling between the free electrons and an external light to form SPPs is not directly possible due to the parallel momenta of SPPs is larger than the free-space light ones for the same frequency. Though, the appearance of nanostructure arrays with determined gratings can provide a source of parallel momentum used by the plasmons to couple to the external field. Moreover, the wide available momenta radiated by TR can also excite these guided waves as well. Therefore, it is generated an excitation of charge-density oscillations in the SPPs confined to the metal surface travelling forth and back and thus, forming standing waves along the nanostructure, which behaves as a resonator. As well, the interaction of the electrons with the metallic material can give rise to electromagnetic far-field components that render coherent to the evanescent external field applied, thus producing electron-induced radiation emission (EIRE).

The excited plasmons can out-couple as electromagnetic radiation components where the emission wavelength is determined by their nature, which in turn depend on the parameters of the nanostructures such as the dimensions, material compositions and the surrounding system [12]. The usual ratio of emission in metals rounds the $3 * 10^{-7}$ SPP per electron per nm SPP wavelength. The SP wavevector can be derived solving the Maxwell equations under suitable boundary conditions yielding a compact final expression (Equation 1).

$$k_{SPP} = k_0 \sqrt{\frac{\epsilon_d \epsilon_m}{\epsilon_d + \epsilon_m}} \quad (1)$$

Where k_0 is the free space wavevector and ϵ_d, ϵ_m are the relative permittivities of the dielectric material and the metal, respectively. It is worth to mention that the larger momentum usually observed in SPP is associated to the binding with the surface. [13].

It is important to mention that even single nanostructures can present antenna properties whether it is possible to control and modify both its electric dipole and higher multipole components [14]. However, the most well-known method to create an

antenna behavior is by means of using a well-defined array of nanoparticles. Regarding suitable parameters, they can jointly enhance and direct strongly spontaneous emissions, moreover, they can control the emission and absorption of light at the nanoscale. Therefore, considering the right parameters, coupling behaviors between light and matter can be observed and, actually, they have been widely studied in many different contexts [6, 15].

After impinging high voltage electrons on a surface, the incoherent emission within the visible wavelengths usually comes from the band-edge electron-hole recombination in nanostructured semiconductors [16] with a suitable band gap or quantum confined nanostructures. The incoherent radiation often emits randomly following a Lambertian distribution [17]. It is important to realize that these excitations tend to be very efficient as one energetic electron can generate a huge number of photons that are excited in cascade. This behavior appears as a limitation factor when we want to measure coherent excitations in CL spectroscopy as the same nanostructure radiates more strongly incoherent than coherent light [11]. As a matter of fact, the sample used in the project has a Si basis, which is a semiconductor accounting a bandgap within the NIR range ($\lambda \sim 1.1 \mu\text{m}$). Thus, CL spectroscopy studies in the visible have remained handy as the Si incoherent emission in the visible is relatively flat, but it has been not possible to extract any valuable information using CL spectroscopy in the NIR range regarding the nanostructures as the luminescence Si peak hugely overlaps all the other resonant peaks.

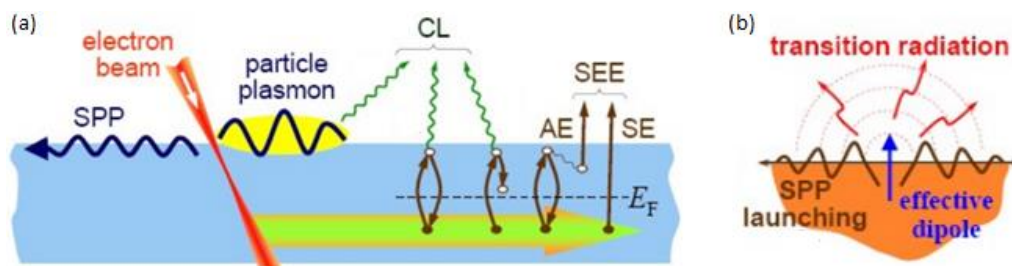


Figure 1. Representation of the different processes that arise when exciting with an electron beam. (a) The electron generates propagating and localized SPPs, the second ones typically decay by coupling to radiation, contributing to CL emission. Moreover, the electron impingement generates electronic excitations in the sample, giving rise to electron-hole

recombination that decay coherently to the same state or incoherently to another one, and both can contribute to CL emission. (b) The transition radiation can also contribute to CL emission, it arises from the cancellation between an electron and its image charge when it crosses a metal surface generating an effective and emitting dipole. Image extracted from the literature [10].

Recent developments in the nanophotonics field regarding high-index dielectric nanoparticles suggest that there are alternative mechanisms to localize light in the subwavelength scale, these are Mie resonances. Mie resonances, which include the Mie optical resonant eigenmodes, consist of electric and magnetic dipoles and higher order hybridized multipoles confined within the high refractive index nanocavities able to generate and control optically induced electric and magnetic responses. Moreover, they can be used to do efficient and unidirectional scattering metamaterials complementing a wide range of plasmonic devices [6].

The eigenmode resonances, which are waves propagating within the nanostructure accounting a certain number of antinodes in each axis, can be derived theoretically from the 3D wave equation. Therefore, the eigenmodes obtained in a nanopillar's geometry for a concrete wavelength are proportional to the product of three sinus, each one is dependent on one axis and gives information about the number of wave's antinodes in that direction. Below, it is shown a general 2D expression of eigenmodes solution in a pillar's cavity.

$$u(x, y) = \sum_{n=0}^{\infty} \sum_{m=0}^{\infty} \sin\left(\frac{(n+1)\pi x}{L_x}\right) \sin\left(\frac{(m+1)\pi y}{L_y}\right) \quad (2)$$

Where $m+1$ and $n+1$ are the number of antinodes presented for the different nanopillar's axis with longitudes L_x and L_y . It is worth to mention that we will consider the $m = 0$ resonance modes seen during the project to be out of plane dipolar modes, that is eigenmodes oriented along the z axis of the nanostructures, regarding that the cavity also holds eigenmodes in the z direction.

The physics related to light scattering by subwavelength particles commonly involves Rayleigh scattering or surface-plasmon interactions that rely on the nature of the materials. In contrast, Mie-type resonances appear when the size of the particles is comparable to the wavelength, which is the case of this project. They can be tuned by

means of modifying both size and geometry of the particles and they do not depend on the material composition [18]. When illuminating with a plane wave, the excitation of a dielectric nanostructure can lead to both electric and magnetic responses with comparable magnitudes and, therefore, the ability to control the phase of transmitted light by controlling them [6].

In the case of nanocylinders, the magnetic resonances arise much stronger than the electric one when $2R \propto \lambda/n$, where n is the refractive index of the material, λ is the wavelength of the incident light and R is the nanoparticle radius [6].

Regarding a Si metamaterial composition, Mie-type resonant modes are mostly confined inside the nanostructures due to the high-refractive index of the material and, moreover, they are poorly absorbed by the material owing to the indirect electronic band presented in Si, thus lending low absorption losses in comparison with plasmonic materials. As a matter of fact, both excited dielectric and plasmonic nanostructures can embed Fano resonances, which are resonances that account an asymmetric scattering profile resulting from the interference between a sharp resonant mode and a broad non-resonant one. In relation to the dielectric nanostructures, Fano resonances are obtainable due to the lower losses presented in high refractive index materials and the contribution of magnetic resonances.

3.2. Cathodoluminescence

Formerly, optical microscopes presented the most powerful way for detecting and analyzing structures in continuously decreasing scales. Though, conventional optical microscopies have a resolution limited by the Abbe's diffraction limit, which states that two points separated less than $d = \frac{\lambda_0}{2NA}$, where λ_0 is the free-space wavelength and NA is the numerical aperture of the microscope, cannot be differentiated. Thus, optical microscopies fail to measure at the true nanoscale when we are in both the Visible (Vis) and Near-Infrared (NIR) range of wavelengths.

Therefore, we use a novel spectroscopy technique based on an electron beam excitation source that copes with the optical diffraction limit, the Cathodoluminescence (CL) spectroscopy, together with a Scanning Electron Microscope (SEM). The CL spectroscopy is based in the collection of CL light emission generated by the target sample due to the

electron beam exposure. An electron beam is an inherently broadband (white) excitation source with a powerful ability to excite any sample regarding that the electrons emitted count on very high momenta. The analyses of CL intensity spectra and CL intensity maps provide detailed information of the resonant modes in the selected area with a nanoscale resolution.

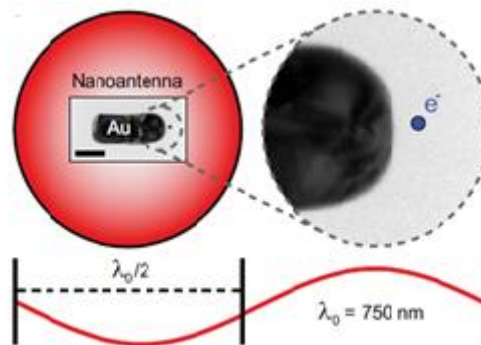


Figure 2. The image, which represents an Au nanorod, illustrates the high resolution of an electron beam spot compared with the limited resolution that offer optical microscopies. Image extracted from the literature [11].

The phenomenon of Cathodoluminescence was first observed in the middle of the 19th century. It was probed that light emission could be generated when the cathode rays (electrons) struck the glass of evacuated discharge tubes. Since then, it has played an important role in the industry; for example, TV screens commonly used this light emission to project. But it has been recently that this phenomenon has been brought to spectroscopy (CL) which, together with a Scanning Electron Microscope (SEM) integrated, constitutes a novel deep-subwavelength resolution spectroscopy technique with a great potential in a lot of fields such as biology and photonics [10].

It is worth to mention that CL spectroscopy can excite both even and odd order resonant modes by means of the high voltage electron beam and detecting the CL resultant emissions using a CCD camera. Moreover, CL spectroscopy is suitable to investigate both optical and plasmonic properties of metamaterials within a deep-subwavelength resolution avoiding contact effects, which could damage the sample. The high resolution of the electron beam is related to the low de Broglie wavelength of the electrons

impinged. If we consider the main used electron beam voltage during the project, that is 30 keV, the wavelength of the electrons can be obtained from Equation 3.

$$\lambda = \frac{h}{(2*m_e*T)^{\frac{1}{2}}} = \frac{6.63*10^{-34}}{(2*9.11*10^{-31}*3*10^4*1.6*10^{-19})^{\frac{1}{2}}} = 7.1 \text{ pm} \quad (3)$$

Where T is the energy of the electron and m_e refers to the electron's mass. Therefore, the small resulting wavelengths of the electrons cope with the resolution limitations into the deep nanoscale.

Depending on the properties of the material, the electric field generated by the electron source can generate different emission responses. The local excitation of the electron beam can excite both symmetric and antisymmetric combination modes regarding an electric or a magnetic nature [19]. Thus, in the visible range of wavelengths it is usual to detect a huge overlapping between modes when analyzing the CL spectrum.

Imaging CL is not only a powerful tool to study localized and propagating surface plasmon resonances through metallic nanostructures but also to study the modes and resonances of any polarizable material including semiconductors and dielectrics. Therefore, it constitutes a good technique to access optical properties regarding a wide range of materials with a nanoscale resolution.

It is important to notice that when the incoming electrons impinge the sample, they scatter and further interact with it creating secondary and backscattered electrons and thus, defining an interaction volume proportional to the acceleration voltage of the source that generates a background signal from the substrate additional to the nanostructure signal.

3.3. Cathodoluminescence Spectroscopy setup

The CL measurements carried on this study have been performed in a Tescan-Delmic SEM-CL spectroscopy. The CL spectroscopy counts on a complex setup. It is principally based on an electron beam that has assembled an aluminum paraboloid mirror with a NA = 0.96 and a focal distance of 0.5 mm in the vacuum chamber of the microscope. The mirror has a 600 μm -diameter hole that allows the electron beam to pass through and impinge the sample, which is situated below. Therefore, the CL emission coming from

the excitation modes that the electron beam has generated on the sample is collected by the mirror and is conducted through a glass vacuum flange to a cooled-Peltier (203 K) silicon 2D charge couple device (CCD) array that works in the Visible range of wavelengths ($\lambda = 400\text{-}900\text{ nm}$).

Moreover, it is essential to assure that each pixel in the CCD camera corresponds to a single point on the paraboloid. The electron beam must hit the sample focused with the mirror accounting the right focus spot size, between 1-10 nm, and correctly positioned in the vertical z-axis with respect to the sample. The alignment is done manually by means of the Odemis Interface. The mirror has attached four piezoelectric stepper motors that allow both translational and rotational movements in it.

Finally, the electron beam scans the selected region of acquisition and the CCD collects the photons rate emitted at each pixel.

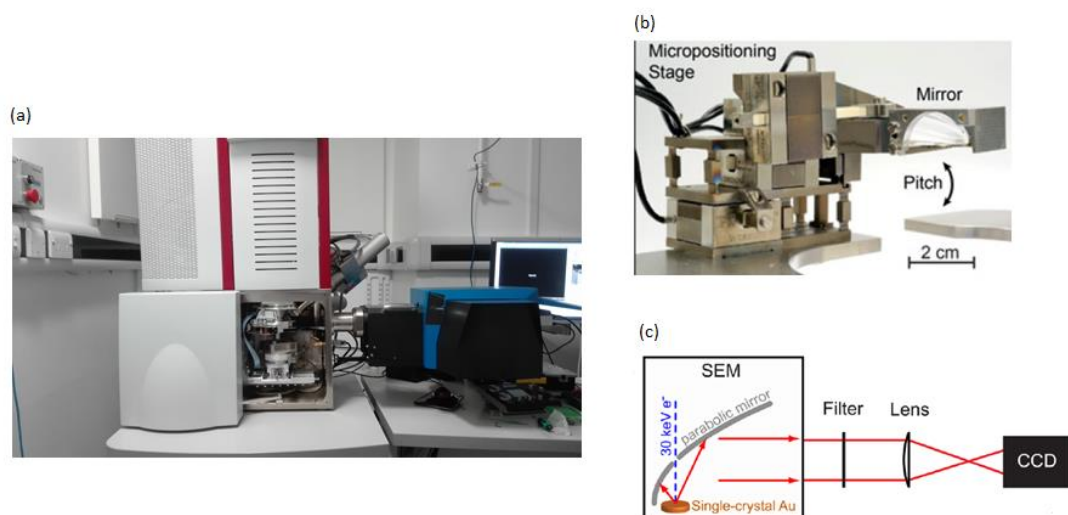


Figure 3. (a) Image of the Tescan-Delmic SEM-CL used. (b) Inside the vacuum chamber, a piezoelectric aluminum-mirror positioning system is mounted, which is used to position a parabolic mirror in four dimensions (x , y , pitch and yaw). (c) Schematic overview of the setup, the sample emission goes through a spectrometer for 2D CL imaging spectroscopy. (b) and (c) images have been extracted from the literature [20], [21].

The Odemis Interface is the software tool used during the CL spectroscopy measurements. It allows to set several parameters to optimize and customize the analysis. Among others, it is used to align the CL electron beam with respect to the

sample and the mirror and to modify the pixel size, the selected region or the electron beam exposure time per pixel.

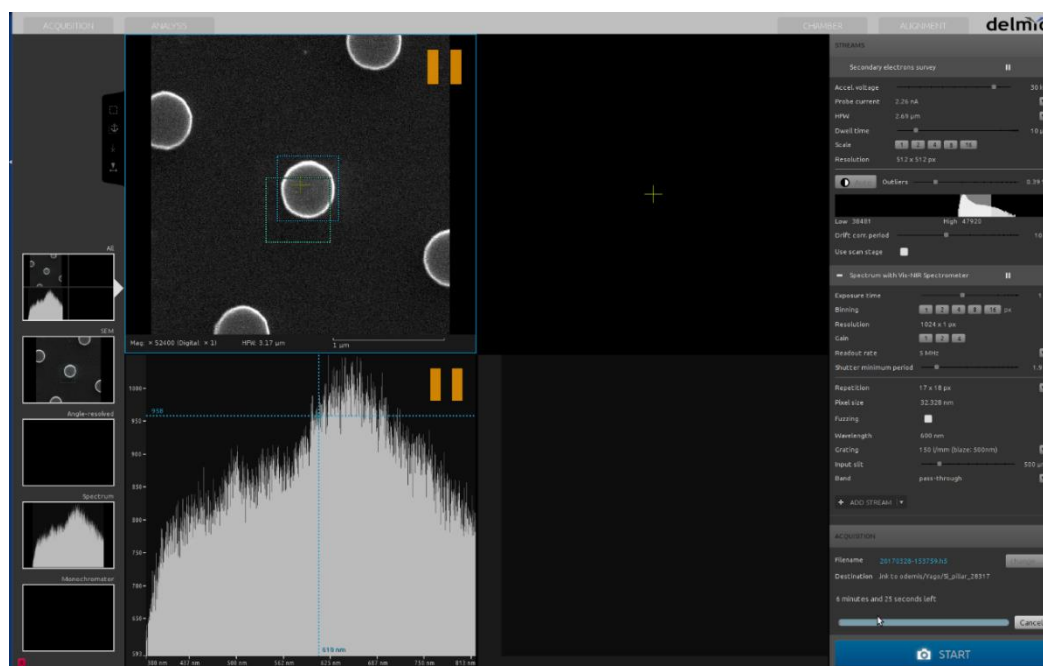


Figure 4. Odemis user interface displaying the custom-made parameters for the analysis such as the pixel size, the beam intensity and the selected region of acquisition.

There are a wide range of voltage and intensity values available in the CL spectroscopy. We will choose the ones more suitable depending on the material composition of the nanostructures and the drifting-resolution agreement that we need for those measurements. Moreover, this technique has integrated a field cancelling system (SPICER CONSULTING SC24) that stabilizes the ambient magnetic field, which are both the Earth's field and the fields radiated by electric power networks and electrical machines, by means of cancelling all other external magnetic fields, therefore improving the microscope performance.

To reduce the drifting effects during the CL spectroscopy acquisitions we must deal with a suitable intensity current and exposure time per pixel. Moreover, the exposure area should be adjusted periodically using the SEM images live recorded. Thus, both CL and SEM images can be directly compared bringing about a powerful correlative technique.

As stated in previous chapters, when the electron beam impinges the sample it does not only excite modes in the nanostructures but it does also excite substrate modes due to

the interaction volume generated, which is proportional to the acceleration voltage. Therefore, the CL emission can be radiated directly by the primary electron beam or by scattered electrons generated in the interaction volume lending a total spectrum that is the sum of both interface excitations.

Regarding that we are interested in the plain nanostructure's emissions, the first approach would be to reduce the acceleration voltage, thus decreasing the interaction volume, but we would lose CL intensity. Therefore, we realize a second acquisition over a plain substrate region and, by means of the Odemis Viewer Interface, we subtract the background substrate CL intensity to the CL spectrum obtained in the nanostructure's region, thus obtaining the pure nanostructure's signal. It is worth to mention that the background is subtracted uniformly which is an approximation from the reality. First, there are impurities and defects in the substrate owing to fabrication imperfections. Moreover, the substrate under the nanostructure will emit less signal than the signal emitted if the electron beam is focused directly on it. Though, these factors are not supposed to generate any relevant change regarding the expected shape and peak resonances of the nanostructures and the approximation remains valid.

We also need to consider that the CCD camera used has a fixed sensibility, which denotes the ability of the photons to be absorbed in the Depletion Region of the detector, not homogeneous in the visible range that will modify the CL intensity spectra obtained. Therefore, the resultant CL spectra must be divided by the relative quantum efficiency function to get the plain CL intensity response of the nanostructure.

The main parameters controlled during the data acquisition are the acceleration voltage (about 30 keV), the intensity beam (about 1 nA), the time exposure per pixel (about 1 sec) and the pixel size, which rounds the 25 nm for the Si nanostructures and the 10 nm for the Au/Si ones. Once the acquisition is done and the background subtraction is realized, we need to normalize the CL spectrum multiplying it by the sensibility inverse function of the CCD camera (Figure 5).

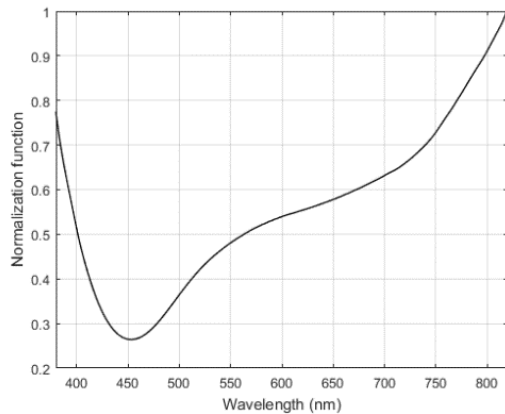


Figure 5. Normalization function extracted from the CL camera's sensibility that must be multiplied by the obtained CL intensity spectrum.

Usually, it is worth to analyze the averaged CL cross section of the nanostructures as well to obtain a different perspective of the resonant mode wavelengths with respect to its spatial position. All the data obtained from the CL spectroscopy is saved in csv and it is analyzed in Matlab 2016b afterwards.

3.4. Optical Spectroscopy setup

The undeniable ability which the CL spectroscopy technique presents to excite a broad range of different modes in the visible range gives us the opportunity to obtain a detailed analysis regarding all the excitation modes present in the nanostructures for these wavelengths. In contrast, the excitation modes usually arise at close wavelengths overlapping each other. Thus, the Optical spectroscopy will be used along the visible range of wavelengths for the Au/Si sample to distinguish the nature of some of the resonant modes encountered in the nanostructures, given that this technique only can excite determined resonances for geometrical reasons. We will impinge light accounting an electric field that can be p or s polarized for different angles of incidence. These measurements will give us more insight whether the resonance has an electric or a magnetic nature or if the dipolar resonances are in-plane or out-of-plane with respect to the surface of the nanostructures.

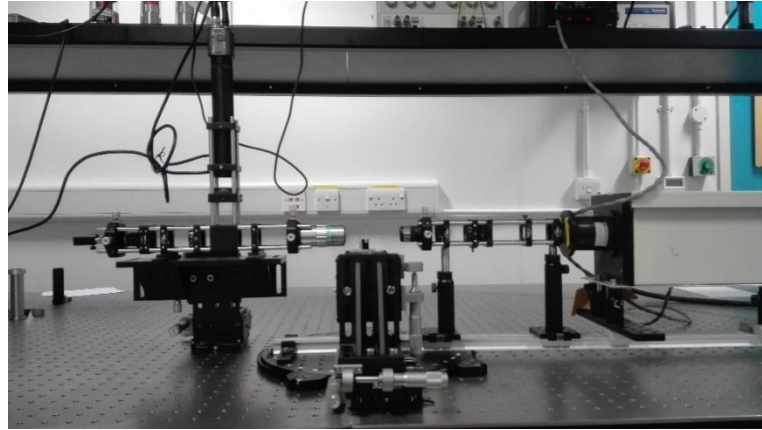


Figure 6. Visible-near IR Spectroscopy setup used in the measurements.

Thus, by means of the Optical spectroscopy we have measured the reflectance intensity percentage within the visible range, setting an incident light accounting an electric field p or s polarized that impinges the Au/Si sample for 30, 45 and 60 degrees with respect to its normal axis. Though the first attempt was to measure the transmission intensity percentage, it was reconsidered because Si is very absorbent in the visible range, and thus, the resultant intensity was expected very low. We can observe slight variations in the intensity spectra obtained for different incident angles owing to the relative height of the nanorods depend on the incident angle as well. Thus, the wavelength positions and the sharpness of the resonant peaks vary in function of the incident angle. It is worth to mention that Local Surface Plasmon Resonances (LSPR), which can arise in plasmonic materials, depend on the (relative) height of the nanostructures [22]. These changes are expected to be small compared with the ones that arise for a determined angle of incidence of the polarized electric field. In relation to the p -polarized incident light, the electric field remains within the incident plane and it can excite both in and out of plane resonances accounting a proper wavelength as it has non-zero components in both axis. Thus, a change in the incident's angle of the light will involve variations in the resonant dip intensities and wavelength positions obtained. In contrast, the s -polarized light, which has an orientation perpendicular to the incident field, only can excite in-plane

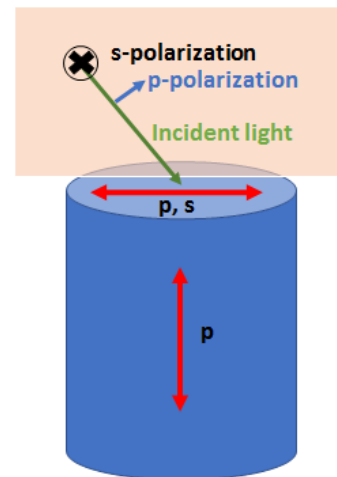


Figure 7. An incident light with p and s polarizations impinges the nanorod. The s -polarization excites only the in-plane modes whereas the p polarization can excite both in plane and out of plane modes.

modes owing to geometrical reasons, it is an orientation mismatch between the out-of-plane and s-polarized waves.

Regarding Maxwell's equations, in an EM wave that propagates through a media, the magnetic field (B) is orthogonal to the electric field (E) and the relation between their magnitudes follows the next expression:

$$B = \frac{E \cdot n}{c} \quad (4)$$

Where n is the refractive index of the medium and c is the speed of light in vacuum. Thus, the light emitted in the Visible spectroscopy will excite predominantly electric resonances as the magnetic field is comparatively weak to excite magnetic modes properly. Thus, we can suppose that the dips encountered in the reflectance intensity percentage spectra present mainly an electrical resonance behavior.

The percentage of total reflected intensity is extracted by means of the next equation:

$$I_t = \frac{I_{sample} - I_{background}}{I_{substrate} - I_{background}} \quad (5)$$

We calculate the background intensity inherent of the setup and the reflected intensity collected when the light impinges the Au/Si plain surface (accounting separated p and s polarizations). Therefore, the total reflected relative intensity is calculated by means of subtracting the background intensity to the intensity obtained from the sample and dividing it by the intensity obtained for the Au/Si plain substrate accounting the subtraction of the background signal one more time.

The data obtained is managed in Origin 9, which is a data analysis and graphing software, and the results obtained are exported in a csv file and processed in Matlab 2016b afterwards.

3.5. Fabrication methods

The sample studied along the project contains a Si substrate that stands Si nanorods and nanopillars embedded in several arrays, in 48 to be precise, accounting different sizes and grating parameters. In each array, the nanostructures have supposedly the same parameters, though in reality, the nanostructures within the same array can present variations in the diameters or sizes of 20 nm at maximum.

The sample was transferred directly by the Plasmonics Group. Its fabrication was carried on by means of an electron-beam lithographic process.

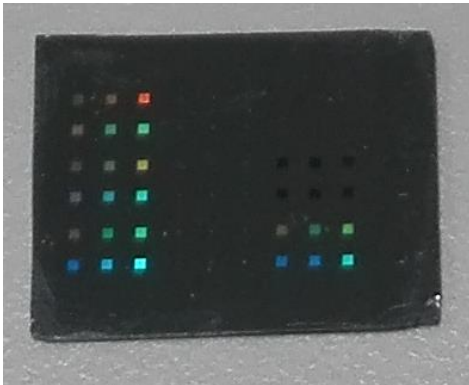


Figure 8. Si sample studied during the project consisting of Si nanostructures embedded in a Si substrate. From this view, it is possible to observe the different wavelengths in the visible range that are captured depending its relative angle with the camera and the array properties [21].

The sample has three different regions as it can be observed in Figure 9. The nanorods present diameters ranging from 290 to 550 nm and their heights are homogeneous (240 nm); thus, the aspect ratios (Diameter/Height) range from 1.2 to 2.5. Regarding the Si nanopillars, they all present sizes from 100 to 600 nm and a constant height of 300 nm. The red dashed region is particularly interesting as the distance between nanostructures is of the order of 100 nm. Thus, we can expect possible couplings arising in the visible range. The grating periods for the white and blue dashed regions are about 1.4 μm . Therefore, we consider that the nanostructures embedded in such gratings are “isolated” in terms of resonance coupling responses owing to the relative large distance of separation between them. All nanostructures height measurements have been realized in an Atomic Force Microscopy (AFM) Bruker Icon Dimension.

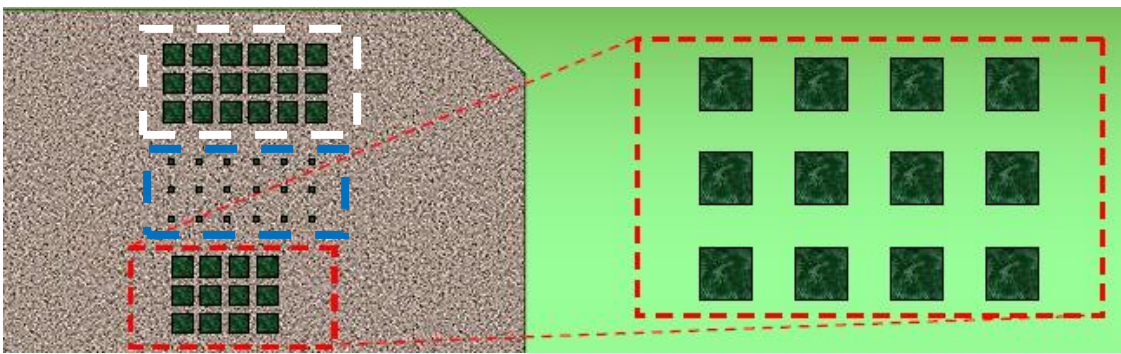


Figure 9. Schematic overview of the Si sample divided by regions. Both the white and blue dashed regions present the same array parameters and nanostructures. They contain 6 arrays of nanorods and 12 arrays of nanopillars. The red dashed region presents 6 arrays of nanorods with a grating period of 1.4 μm and 6 arrays of nanopillars with grating periods of 300 nm.

Once the study regarding the Si sample is completed, the next part of the project consists on recovering the entire sample with an Au layer accounting a thickness of 35 nm to study the different resonances arising for these new parameters, in the visible range as well.

Gold is an interesting material to study in CL spectroscopy for several reasons. Though it is usually high reflective, at the nanoscale it can be a great absorber of light for suitable parameters. What is more, this light is absorbed by the free electrons localized in the surface of the metal giving rise to surface plasmonic resonances (SPRs) [13]. Thus, we will study both SPRs and Mie optical resonances in the sample arising from the Au layer and the Si core.

The Si sample was Au-covered by Dr. Wayne Dickson by means of sputtering (PVD 75 Magnetron Sputtering), a physical vapor deposition technique that consists on ejecting Au nanoparticles from an Au target to the Si sample using an accelerated ion gas. The thickness of the Au layer is fixed to 35 nm. Though the Au deposition is randomly located in the sample, at the end of the procedure it is fair to consider that a roughly homogeneous covering has taken place. In agreement, AFM measurements done for the Au/Si sample have revealed that the heights of the nanostructures remain constant (at 240 nm and 300 nm for nanorods and nanopillars, respectively). Nevertheless, after the Au deposition, the distance between the nanostructures has decreased regarding the Au deposition at the edges which is not homogeneous in turn, lending increments in the particle sizes.

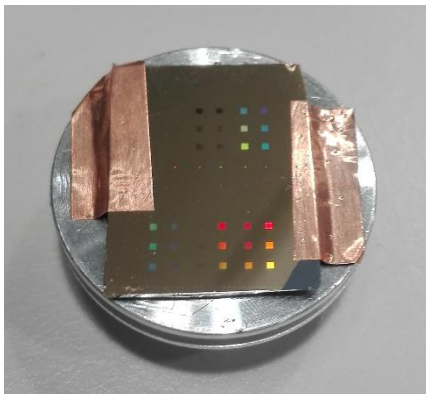


Figure 10. Si sample covered up with an Au layer. The Copper (Cu) thin layers attached aim to increase the conductivity of the sample to obtain a better intensity signal in the CL spectroscopy.

3.6. COMSOL Multiphysics modeling

Along this project it has been developed a model in COMSOL Multiphysics, which is a general-purpose software platform based on advanced numerical methods, to simulate the experimental CL intensity spectra and the resonance peaks obtained using CL spectroscopy in both Si and Au/Si nanorods. Therefore, we simulate the averaged outflow power emitted by both Si and Au/Si nanorods when they are excited by a line current. We consider the nanorods isolated standing in its respective substrate, Si or Au/Si respectively. Regarding that the CL intensity and the outflow power are related but do not have the same units, we present the normalized functions over its maximum to compare them faithfully.

The simulation procedure can be separated in different sections. Firstly, we start building the nanostructures (Si nanorods in a Si substrate) with the desired size and defining the material properties such as Si, air (considered as vacuum to simulate the vacuum chamber where the sample is held during the CL measurements) and Au if necessary. In relation to the Au/Si nanorods, it has been considered an Au layer 35 nm-thick which covers both the substrate and the top of the nanorod. Moreover, it is considered a 10 nm-thick Au homogeneous layer deposition on the lateral surface of the nanorod. It is important to mention that the lateral Au deposition is not homogenous at all and the approximation could carry slight or moderate possible mismatches in the simulations when compared to the experimental results.

The simulations aim to study the behaviors of the nanostructure resonances in the visible range of wavelengths when they are excited along different positions. Thus, we have considered the frequency domain and the Maxwell's derived equations for the electric field within the domains:

$$\nabla \times \mu_r^{-1} (\nabla \times \mathbf{E}) - k_0^2 \left(\epsilon_r - \frac{j\sigma}{\omega\epsilon_0} \right) \mathbf{E} = \mathbf{0} \quad (6)$$

Moreover, the electric field follows the corresponding expression in the boundaries derived from Maxwell's equations as well:

$$\mathbf{n} \times (\nabla \times \mathbf{E}) - jk\mathbf{n} \times (\mathbf{E} \times \mathbf{n}) = -\mathbf{n} \times \left(\mathbf{E}_0 \times (jk(\mathbf{n} - \mathbf{k}_{dir})) \right) e^{-jk\mathbf{k}_{dir} \cdot \mathbf{r}} \quad (7)$$

Both the refractive index (n) and the extinction coefficient (k) for Au and Si in the visible range used in the model have been extracted from the wide-used literature [23, 24]. Therefore, we can calculate the relative permittivity (ε) from n and k by means of the next expression:

$$\varepsilon(\omega) = n^2 - k^2 - 2ink \quad (8)$$

Where n , k and ε are wavelength-dependent. The relative permeability of both materials is considered 1 and the electrical conductivity is set to 0 as the imaginary part of the relative permittivity calculated does include this term.

The excitation source considered in the model is quite efficient regarding our necessities, it is a line current oriented parallel to the vertical axis of the nanorod serving as an electron source instead of using a point dipole, the common excitation source used in these situations. This approach will allow us to compile information of the z axis while the line current moves along the x - y plane, saving a considerable amount of computational time. The line current must be the same length as the nanorod and it must be totally embedded in the nanostructure owing to the interaction of the electrons generated in the line current do not interact with air. The line current radiates a cylindrical wave able to excite both electric and magnetic resonances in the nanostructures. To simulate a spatial resonant spectrum, we make the line current to sweep from the center ($r = 0$) to almost the edge of the nanorod, lending a minimum distance of 8 nm between the edge and the end of the sweep to avoid possible meshing inconveniencies. Moreover, we consider a radial resonance symmetry; thus, it is enough to sweep the line current along a straight line in 1D to give a 2D information of the resonant behaviors. We usually calculate over 7 different equidistant points, from the center to the edge of the nanorod.

All domains are properly meshed considering an element size of 60 nm, exempting the cylinder that surrounds the line current, where the outflow power is integrated, which has an element size of 3nm. These meshing sizes present a good compromise between computational time optimization and exactitude giving a maximum of 5% relative error with respect to the most accurate mesh analyzed.

The wavelengths calculated range from 400 to 800 nm in steps of 5 nm. The simulations solve the averaged outflow power emitted by the system for the ordered positions and wavelengths. All the results are saved in a csv file and analyzed in Matlab 2016b afterwards. The average power spectra are finally normalized multiplying them by the Si background CL intensity spectrum for the Si nanorod simulations or by the Au/Si CL background intensity spectrum for the Au/Si nanorod simulations, replacing the homogeneous intensity considered (1 A) for the proper one in each case.

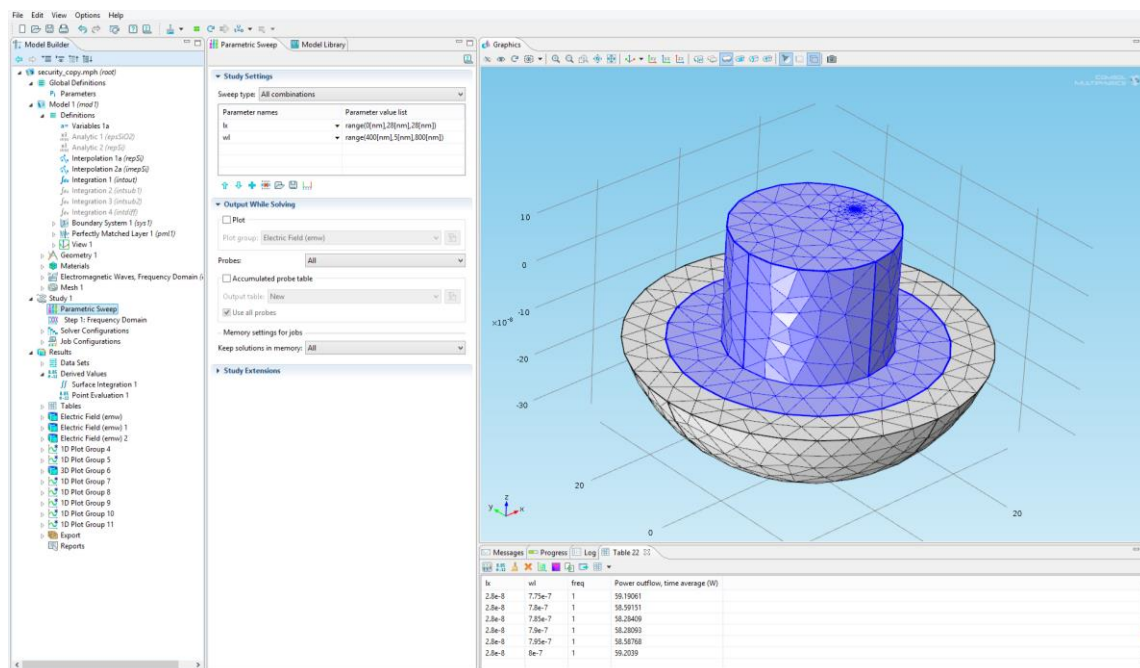


Figure 11. COMSOL Multiphysics 4.3b user interface displaying the custom-made parameters and geometries for an Au/Si nanorod.

4. Results and Discussion

In this chapter, we present all the results obtained in CL spectroscopy, Visible Spectroscopy and COMSOL simulations and the corresponding discussions. Depending on the section, we study the nanostructure resonances using one or more of the already mentioned techniques, regarding that CL spectroscopy is the technique used for excellence in this project and the other methods, when applied, complement and give a further insight to the CL results obtained. During all the CL measurements done, we always use a 30 keV electron beam and we work within visible wavelengths (from $\lambda = 400$ nm to $\lambda = 800$ nm).

The CL spectroscopy technique is very useful to excite and analyze most of the resonant modes presented in nanorods and nanopillars accounting different sizes, gratings and material compositions in the visible range of wavelengths. Thus, it gives us detailed information about all the resonant modes presented in the nanostructures. However, the different resonant modes appear usually overlapped within the visible range of wavelengths losing clarity to explain and observe them by means of the CL maps and CL intensity spectra. The model proposed in COMSOL aims to simulate faithfully the resonant peaks obtained experimentally using CL spectroscopy. Moreover, the Visible spectroscopy will let us know about the presence of a Fano resonance in one of the arrays for Au/Si sample where there are couplings between nanopillars, thus increasing the insight in the behaviors of the system with resonances.

In order to analyze as much accurately as possible the resonant behaviors encountered in the nanorods, it is considered an analytical model obtained from published data that describes the resonant Mie-like optical eigenmodes and photonic wavefunctions for Si 2D disk resonators in a SiO₂/Si substrate [25]. This model has resulted to be very helpful to explain the nature of the resonances for both Si and Au/Si nanorods when compared with the experimental results.

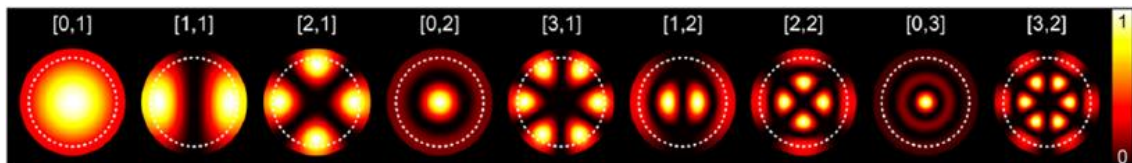


Figure 12. Photonic wavefunctions for different azimuthal and radial modes respectively, the first term that appears in the square brackets refers to the azimuthal number (m) and the second, to the radial number (q). The azimuthal terms determine whether the resonance is dipolar, quadrupolar or octupolar and the radial term gives information about the order of the mode. In this image is plotted the time average amplitude $|E_z(r, \varphi)|^2$. Image extracted from the published data already mentioned [25].

4.1. Silicon nanostructures

The CL intensity maps obtained for the Si nanostructures present a quite low resolution, it is a relatively large pixel size (around 25-30 nm), which arises principally owing to the bad conductivity of Si. Moreover, the high refractive index of the Si ($n \cong 4$ in the visible

range of wavelengths) procures that a major portion of the light gets scattered into the substrate (around 90 %) where it cannot be detected, and its indirect band gap induces a relatively weak fundamental CL emission compared to the semiconductors generated with defects as it is required a phonon emission for an electron-hole pair recombination [16].

4.1.1. "Isolated" nanorods

In the next pages CL intensity spectra, CL intensity maps and the proposed COMSOL model simulations are shown and discussed for three Si nanorods with different diameters (320, 400 and 500 nm) and a homogeneous height (240 nm).

As explained in the previous section, Si nanostructures usually show drifted images in the CL spectroscopy acquisition, generating non-reliable data. Thus, to overcome the problem, we must decrease the exposure time per pixel and increase the pixel size, sacrificing resolution and signal to noise ratio in the results. It is worth to mention that the low resolution obtained for the Si nanostructures makes it difficult to distinguish higher order modes only looking at the CL maps, but the analytical model extracted from published data will help us to describe the different resonant behaviors encountered.

We have done the CL spectroscopy analysis accounting an intensity current of 1.13 nA, a pixel size of 30 nm on average and an exposure time per pixel of 1s. The CL intensity maps have been averaged over a 15 nm-bandwidth to obtain a clearer response. The color scale represents the normalized CL emission intensity.

In relation to the 320 nm-diameter nanorod, Figure 13a shows the normalized CL intensity spectra averaged over all the top surface (blue line) and averaged over a handful of pixels situated at the center of the surface (black line). The whole surface averaged spectrum reveals the high overlapping between modes that count on similar intensity peaks as none stands out the others. The center averaged spectrum, though, shows a clear resonant peak at $\lambda = 650$ nm and the starting of another one for $\lambda = 400$ nm. This centered spatially integrated spectrum allows us to distinguish to some extent the $m = 0$ out of plane dipolar resonances, regarding that they are excited more efficiently in the center.

To compare the experimental resonant peaks obtained with the numerical simulated results extracted from the COMSOL model proposed, we plot the normalized outflow power in function of the wavelength as it is shown in Figure 13b, regarding both the total averaged spectrum (averaged over all the positions calculated in the nanorod) and the spectrum calculated just at the center position of the nanorod (blue line and black line, respectively). We observe that the model represents quite well the resonant peak distributions and relative intensities despite, in some cases, the simulated resonant peaks are quite broader than the ones obtained experimentally. In relation to the center averaged spectrum we can note a sharp dip for wavelengths around $\lambda = 750$ nm while in the experimental results the intensity decreases but quite more smoothly, and the simulated intensity peak is slightly blue-shifted with respect to the experimental one. The low resolution of the experimental results has brought about to some extent the discrepancies observed with respect to the simulated results. Regarding that the pixel size considered is 30 nm and the CL intensity center averaged spectrum is taken for a handful of pixels situated at the center, the experimental center considered is much wider than the considered in the simulations, which only contemplates 3 nm of radius surrounding the exact center of the nanorod's top surface (the cylinder that surrounds the line current used in the simulations has a radius of 3 nm).

To characterize the spatial mode profile, Figure 13 (c-f) shows the CL intensity maps at the wavelengths that correspond to the resonant peaks obtained. It is worth to mention that both the CL intensity center-averaged spectrum and the CL maps presented experimentally in this work are similar to the ones obtained for published data accounting a Si nanorod of 321 nm-diameter and 100 nm-height in a SiO₂ substrate [25]. As a matter of fact, the resonant peak positions displayed in our nanorod resemble to the published one as well. Thus, we can note that the height of the nanorod and the change from silica (SiO₂) to silicon substrates have a minor CL intensity spectrum impact with respect to a change in the diameter. For $\lambda = 400$ nm the CL intensity is maximum at the center and at the edges of the nanorod's surface; thus, we can observe the possible hybridization of an $m = 0$ out of plane high-order dipolar resonance ($\{m = 0, q = 4\}$) and an $m = 2$ quadrupolar mode $\{2, 3\}$, (see Figure 12 to observe the relatively well matching between all the eigenmodes experimentally obtained during the analyses and the

photonic wavefunctions expected in the analytical model). For $\lambda = 550$ nm there is a dominance of the hybridized $\{3, 1\}$ (octupolar mode) and $\{1, 2\}$ (higher-order dipolar in plane mode) resonances. At $\lambda = 650$ nm the CL intensity is by far maximum at the center of the nanorod in agreement with both the experimental and simulated spectra displayed in Figure 13 (a, b), it is the hybridization of a $m = 0$ out of plane dipolar resonance and a quadrupolar resonance ($\{0, 2\}, \{2, 1\}$). For $\lambda = 750$ nm it is observed a hybridization between the first order dipolar out of plane and in plane resonances ($\{0, 1\}, \{1, 1\}$). These two resonances arise at quite close wavelengths and thus, it is relatively easy to observe their hybridization. As it can be observed, higher order resonances appear for shorter wavelengths.

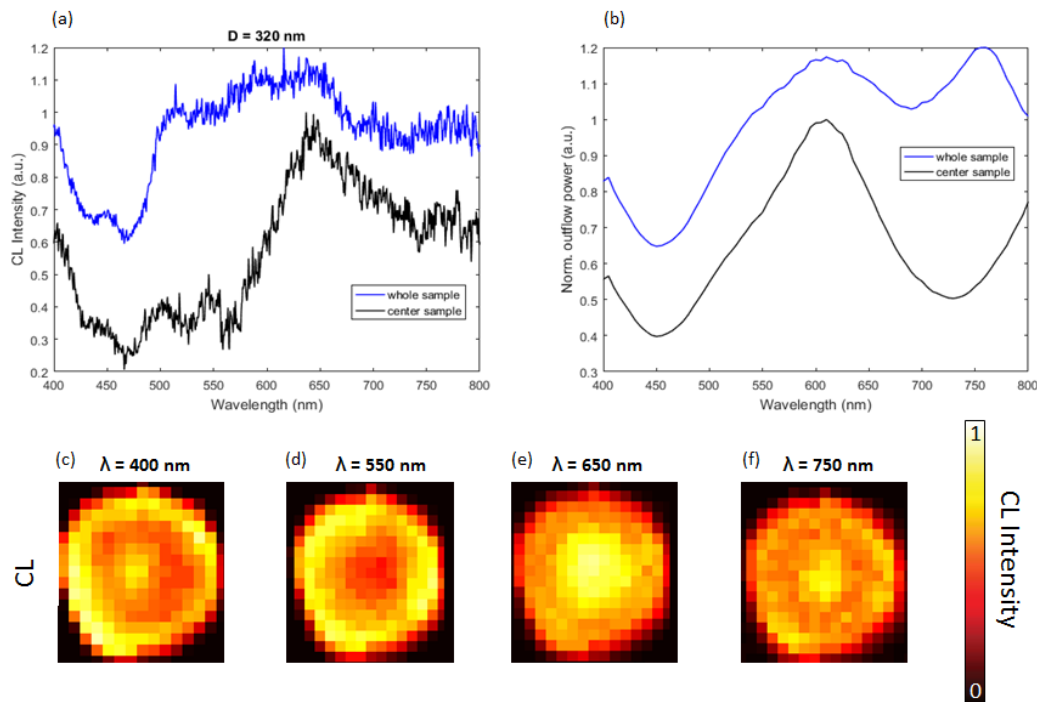


Figure 13. Full compilation of CL Intensity spectra, CL maps and COMSOL simulations for the 320 nm-diameter nanorod. (a) Normalized CL intensity spectra averaged over all the surface (blue line) and center averaged (black line) in function of the wavelength. The y axis has been cut off for clarity. High overlapping of modes observed for the total averaged spectrum (blue line). (b) COMSOL-simulated normalized outflow power spectra averaged over all the sweep points of the nanorod (blue line) and obtained just at its center (black line). Quite well matching between the experimental and the simulated results. (c-f) CL intensity maps

integrated over a 20 nm-bandwidth showing the resonant mode peaks obtained in (a) and (b) for (c) $\lambda = 400$ nm, (d) $\lambda = 550$ nm, (e) $\lambda = 650$ nm and (f) $\lambda = 750$ nm.

Figure 14 shows the same analysis represented in Figure 13, but for the 400 nm-diameter nanorod. The CL intensity spectra presented in Figure 14a seem less overlapped than for the 320 nm-diameter nanorod, regarding that three resonant peaks stand out from the rest for $\lambda = 560, 660$ and 770 nm in both the whole averaged and the center averaged CL intensity spectra. The COMSOL simulations of the model proposed (Figure 14b) follow quite well the shape of the experimental CL intensity spectra obtained, though, with some slight shifts in some of the wavelength peaks. The normalized simulated outflow power shows the resonant peaks more overlapped and less clear than the experimental ones for this case. It is worth to mention that in the model we only excite and calculate about 7 different positions from the center to the edge of the nanorod to save computational time, which of the order of days. Therefore, the simulations show an approximate response in some cases with respect to the experimental intensities obtained.

In Figure 14 (c-f), the CL intensity maps are displayed at the resonant peak wavelengths. For $\lambda = 560$ nm the CL emission is maximum at the center and at the edge of the nanorod's surface; thus, we can observe the hybridization of an $m = 0$ out of plane high-order dipolar resonance ($\{m = 0, q = 3\}$) and an $m = 2$ quadrupolar mode $\{2, 2\}$, (see Figure 12 to observe the matching between all the eigenmodes experimentally obtained during the analysis and the photonic wavefunctions expected in the analytical model). For $\lambda = 620$ nm, we observe a dip of emission at the center of the nanorod's top surface that owes to a possible hybridization of a $\{3, 1\}$ octupolar mode and a $\{1, 2\}$ higher-order dipolar resonance mode, in agreement with the analytical model coherence. For $\lambda = 660$ nm the CL intensity is not well defined, partly due to the low resolution. It seems to present two bright spots near the center which could mean the dominance of an $\{1, 2\}$ dipolar second order mode. For $\lambda = 750$ nm it can be observed the dominance of an $m = 0$ resonant mode as the center is more efficiently excited, pointing at a $\{0, 2\}$ resonant mode being consistent with the expected results from the analytical model considered.

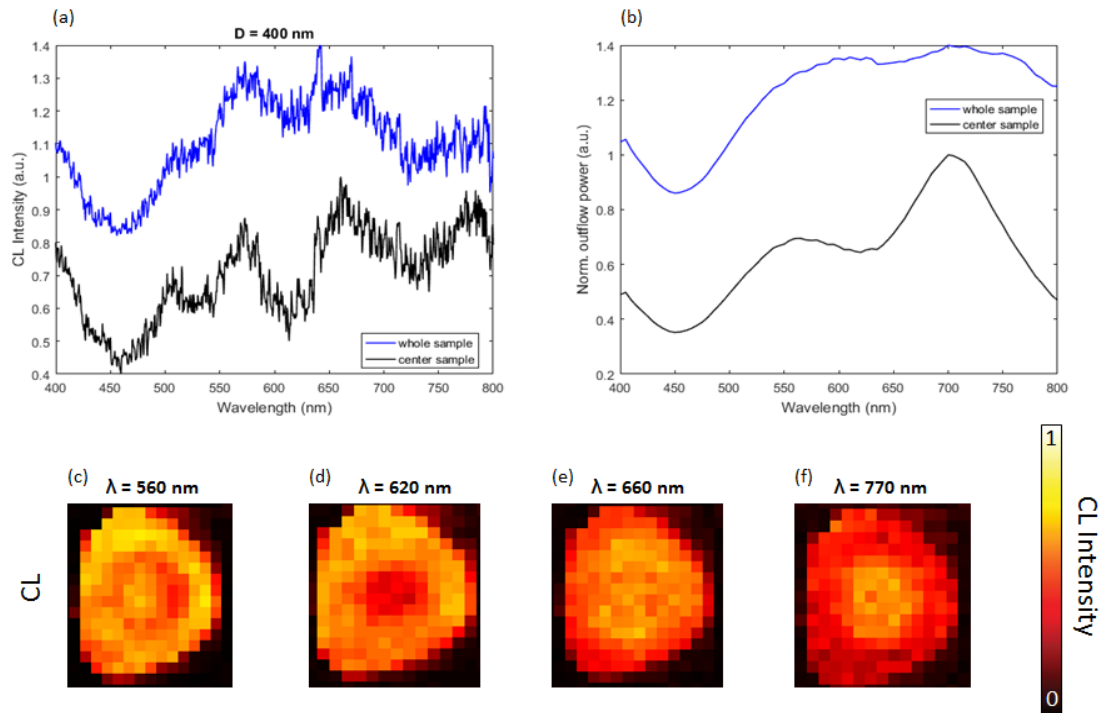


Figure 14. Full compilation of CL Intensity spectra, CL maps and COMSOL simulations for the 400 nm-diameter nanorod. (a) Normalized CL intensity spectra averaged over all the surface (blue line) and center averaged (black line) in function of the wavelength. The y axis has been cut off for clarity. Three resonant peaks observed for $\lambda = 560$, 660 and 770 nm in both different spatially averaged CL intensity spectra. (b) COMSOL-simulated normalized outflow power spectra averaged over all the sweep points of the nanorod (blue line) and obtained just at its center (black line) in function of the wavelength. Fair matching between experimental and simulated results, the simulated responses are more overlapped than the experimental ones. (c-f) CL intensity maps integrated over a 20 nm-bandwidth showing the resonant mode peaks obtained in (a) and (b) for (c) $\lambda = 560$ nm, (d) $\lambda = 620$ nm, (e) $\lambda = 660$ nm and (f) $\lambda = 770$ nm.

In Figure 15 it is shown a detailed analysis for the 500 nm-diameter nanorod. The CL intensity spectra averaged over the whole surface shown in Figure 15a (blue line) is the sum of many overlapped resonant peaks. They arise clearer in the CL intensity spectrum center averaged in Figure 15a (black line) where we can observe two resonant peaks standing out at $\lambda = 640$ and 750 nm. COMSOL simulations done (Figure 15b) keep the same overall shape but again the resonant peaks appear more overlapped than in the experimental results (regarding that the shift observed in the resonant peak wavelengths comparing the respective experimental and simulated center averaged spectra has been already explained).

In Figure 15 (c-f), the CL intensity maps are displayed for resonant peak wavelengths. In Figure 15 (c, d and f) it can be observed a bright spot in the center that reflects the dominance of an $m = 0$ dipolar mode hybridized with other modes that account higher orders for shorter wavelengths. Figure 15e shows a CL intensity map that seems dominated by an $m = 1$ higher order dipolar mode quite hybridized, but it is no clear. For this nanorod, we have not used the analytic model extracted from published data [25] to explain the nature of the different resonant modes obtained, regarding that the nanorod's diameter ($D = 500$ nm) is quite large and it stands higher-order modes not presented.

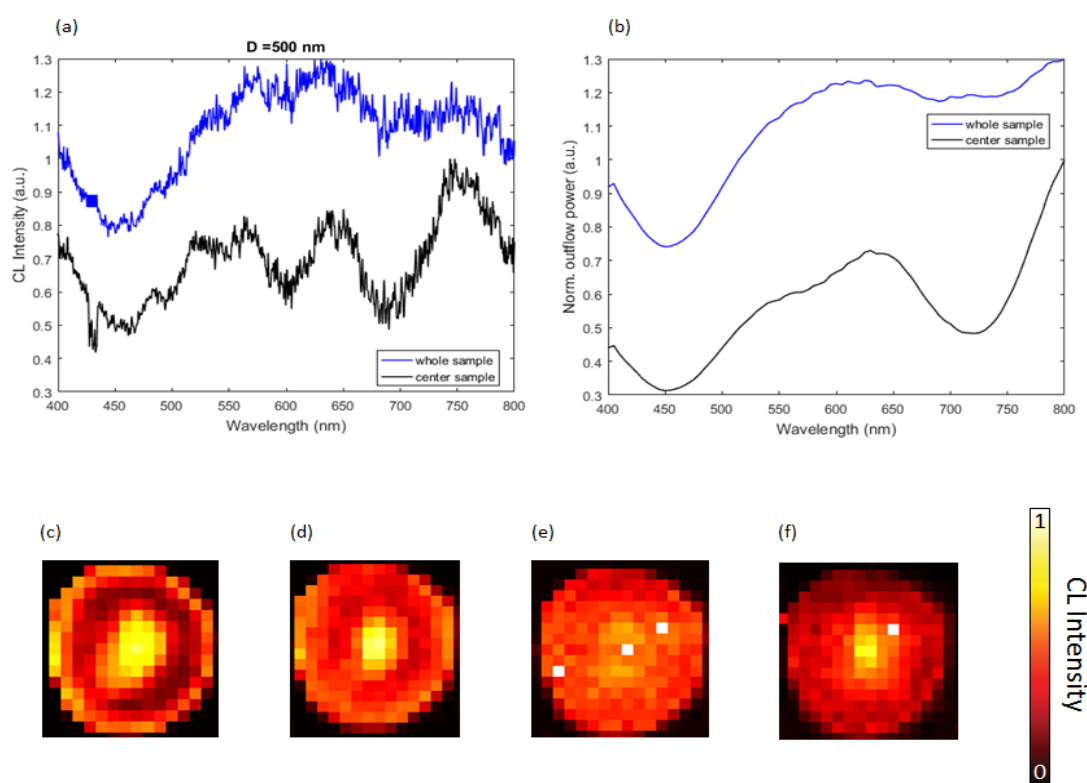


Figure 15. Full compilation of CL Intensity spectra, CL maps and COMSOL simulations for the 500 nm-diameter nanorod. (a) Normalized CL intensity spectra averaged over all the surface (blue line) and center averaged (black line) in function of the wavelength. The y axis has been cut off for clarity. Huge overlapping of modes shown in the whole averaged CL spectrum. Two peaks stand out for the center averaged CL spectrum at $\lambda = 640$ and 750 nm. (b) COMSOL-simulated normalized outflow power spectra averaged over all the sweep points of the nanorod (blue line) and obtained just at its center (black line) in function of the wavelength. The resonant CL spectra shapes match quite well with the experimental ones though they appear more overlapped. (c-f) CL intensity maps integrated over a 20 nm-bandwidth showing

the resonant mode peaks obtained in (a) and (b) for (c) $\lambda = 400$ nm, (d) $\lambda = 550$ nm, (e) $\lambda = 640$ nm and (f) $\lambda = 750$ nm.

It can be clearly noted if we compare Figure 13d with Figure 14d and Figure 13e with Figure 14f that an increment in the diameter causes a progressively red-shift to the resonant mode wavelengths encountered as one could expect for geometrical resonances [26]. Moreover, this red-shift in the wavelength brings about the appearance of higher-order modes for larger diameters in the visible range.

The model proposed in COMSOL for isolated Si nanorods in a Si substrate gives a first fair approach to simulate the resonant peaks obtained in CL spectroscopy accounting a 30 keV electron beam. Though, further research is needed in the field to improve the model making it more realistic, for example, by considering several moving vertical point dipoles sweeping for different positions instead of a line current.

As it can be observed in Figures 13, 14 and 15, the CL intensity spectra averaged over the whole surface show quite similar responses in the visible wavelengths. It owes to the huge overlapping of resonant peaks at the same range of wavelengths that only allows to see a broad intensity peak in many cases. Thus, the CL intensity spectra calculated averaging for a handful of pixels situated at the center of the nanorod aim to show some of the resonant peaks clearer and less overlapped.

All the CL intensity and normalized outflow power spectra obtained in the analysis of Si nanorods present an emission dip for wavelengths centered in $\lambda = 450$ nm. It owes to Si has a larger absorption for blue wavelengths, thus lending higher absorption losses that involve a decrease in the intensity spectra obtained in the blue.

4.1.2. "Isolated" nanopillars

In relation to the resonant behavior analyses for the Si nanopillars, 3 different ones have been selected with an equal height of 300 nm and accounting different sizes: 340 x 500, 300 x 380 and 280 x 320 nm.

In the CL analyses, we raster scan the electron beam (1.13 nA current intensity) over the surface of the nanopillars taking a pixel size of 25 nm and considering an exposure time of 1s per pixel. It is worth to mention that nanopillars present less symmetry than

nanorods, so the resonances are going to be observed more accentuated especially in the edges of the nanostructures. Figure 16 shows the spatial CL intensity maps for an averaged bandwidth of 15 nm. As it can be observed and it has been stated in the theory, these Si nanopillars act as nanocavities confining the light within the nanostructures. Thus, the resonances observed in the CL maps are dominated by Mie optical eigenmodes confined within the nanopillars. In Figure 16b it can be observed a 3D image of the nanopillar's array taken in the AFM, technique that we have used to measure the height of all the nanostructures analyzed.

Regarding the 340 x 500 nm nanopillar, we can observe in Figure 16a and Figure 16i a centered bright spot for $\lambda = 484$ nm and $\lambda = 787$ nm. This efficient excitation in the center owes to the dominance of a possible $m = 0$ resonance. The different $m = 0$ excitations present a higher order for the lower wavelengths. In Figure 16f it is shown the predominance of a $m = 1$ in plane dipolar resonance through the long axis of the nanopillar at $\lambda = 691$ nm. Figure 16c shows, though not clearly, a presumable apparition of an $m = 2$ resonant mode through the long axis and an $n = 1$ mode through the short axis of the nanopillar for $\lambda = 617$ nm. The distance between the antinodes (bright peaks) matches approximately half the wavelength of the resonant modes as it was expected for the eigenmode resonances.

In relation to the 300 x 380 and 280 x 320 nm nanopillars, we can distinguish the same resonances that have arisen for the largest nanopillar but accounting blue-shifted wavelengths. An azimuthal symmetric resonance $m = 0$ seems to dominate in Figure 16j and Figure 16k for the 300 x 380 and 280 x 320 nm nanopillars, respectively at $\lambda = 682$ and 658 nm.

Considering the 300 x 380 nm nanopillar, it can be observed in Figure 16g a clear dominance of an $m = 1$ resonance through its long axis for $\lambda = 624$ nm. Figure 16d seems to show for $\lambda = 554$ nm another $m = 1$ dominant resonance along the long axis of the nanopillar and an $n = 1$ resonance along the short axis, but the image is not completely clear due to drifting effects and a quite low resolution.

In relation to the 280 x 320 nm nanopillar, Figure 16 (e, h) shows again the dominance of two different in-plane dipolar resonances, $m = 1$, at $\lambda = 508$ and 577 nm (blue-shifted

with respect the 300 x 380 nm nanopillars as expected), where the edges are most efficiently excited.

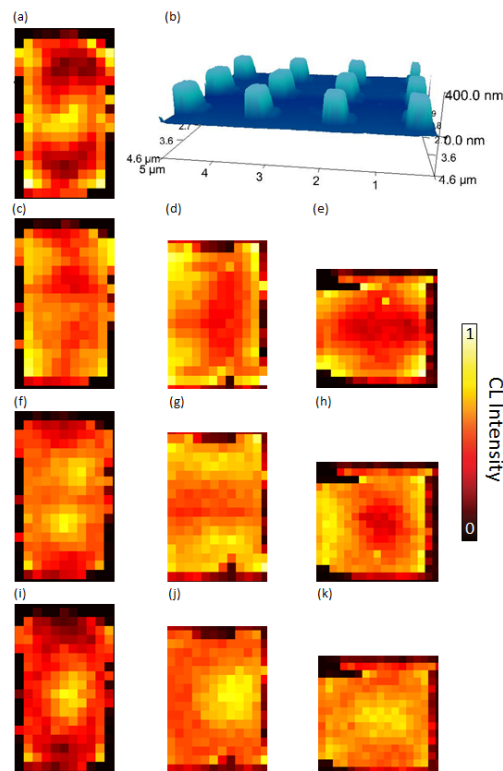


Figure 16. CL normalized emission maps of Si nanopillars in a Si substrate. From left to right column, the sizes of the nanopillars are: 340 x 500, 300 x 380, 280 x 320 nm respectively, and the height is 300 nm, homogeneous along all nanopillars. (b) AFM Image that shows the array of nanopillars. (a) $m = 0$ dominant resonance at $\lambda = 484$ nm. (c) $m = 2$ (long axis), $n = 1$ (short axis) dominant eigenmode resonance for $\lambda = 617$ nm. In the second row (d-e) it is observed an $m = 1$, $n = 1$ dipolar resonance for $\lambda = 554, 508$ nm from left to right. The third row (f-h) shows an $m = 1$ in-plane dipole along the large axis of the nanopillars at $\lambda = 691, 624, 577$ nm from left to right. In the last row (i-k) it can be seen a bright spot in the center of the nanostructures meaning a possible dominance of an $m = 0$ resonance behavior for $\lambda = 787, 682, 658$ nm, respectively from left to right.

To compare quantitatively the intensity peaks and the wavelength positions for the resonant eigenmodes encountered for each nanopillar, we show in Figure 17 the normalized CL intensity spectra averaged for a handful of pixels localized at the center of the nanostructures to compare the resonances whose dominance is rendered for an $m = 0$ eigenmode excitation, regarding that they are excited more efficiently in the center. It is observed a red-shift in the main intensity peak wavelengths for increasing

nanopillar sizes, in agreement with the CL maps already visualized. Moreover, we can observe an $m = 0$ predominant resonance for the largest nanopillar at a wavelength rounding the $\lambda = 400$ nm and the beginning of possible $m = 0$ resonances at wavelengths about $\lambda = 380$ nm for the shorter nanopillars.

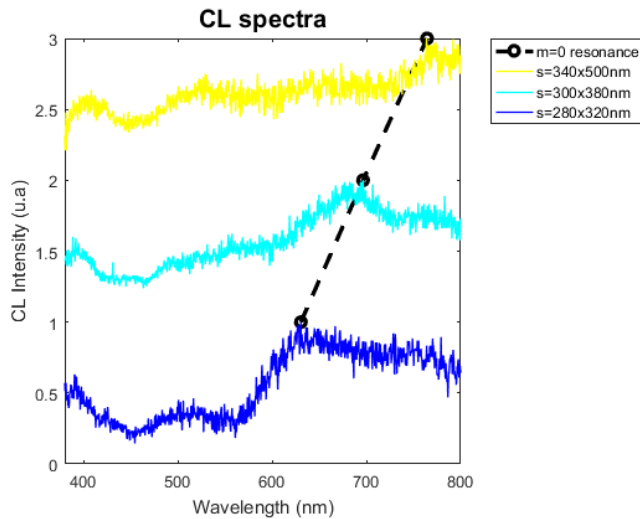


Figure 17. Spatially centered averaged CL spectra for different nanopillar sizes. The normalized intensities have been vertically offset for clarity. The dominant resonances show a clear red shift in wavelengths for larger nanopillars.

4.1.3. “Non-Isolated” nanopillars

It is widely known that an array of nanostructures standing close enough each other can experiment couplings between them able to radiate in the far field. Therefore, setting suitable sizes, distances between nanostructures and material compositions we can promote an array to direct and enhance radiative emission or, otherwise, to confine light in the nanoscale.

Regarding that the nanopillars itself present a large collection of geometrical mode resonances, the couplings bring about a broad range of hybridized modes, giving rise to even more resonant peaks with strong spectral overlap. As a matter of fact, each nanopillar situated within the array adds a resonant peak to the spectrum. Ideally, if there were no losses, we would be able to distinguish all the sharp peaks in the spectrum. In contrast, we can observe in Figure 24, which shows the CL intensity spectrum calculated for an Au/Si nanopillar embedded in an array with couplings, a broad band peak that is the sum of all the resonant peaks. It is important to mention that the couplings presented in this array are quite weak because there is still a large distance between nanopillars (180 nm along the short axis of the nanopillar and 70 nm along the large axis) [19].

An array of Si nanopillars with a close distance between them is analyzed by means of CL spectroscopy, scanning the electron beam (788 pA intensity current) over the surfaces of the nanopillars, taking a pixel size of 20 nm, an exposure time of 1s per pixel and averaging the CL intensity maps over a 20 nm-bandwidth. It is worth to mention that the nanopillars embedded in the array have similar sizes and thus, the same or similar resonant modes and wavelength should be expected whether they did not experiment any coupling behavior.

In Figure 18e it is shown a SEM image regarding one region of the nanopillar's array. We can observe in Figure 18 (a-d) two clear dominant resonant modes over the complex hybridized higher order modal profiles in both nanopillars. Figure 18 (a, c) shows the normalized CL intensity maps of the nanopillar standing at the vertex of the array (150 x 230 nm) for (a) $\lambda = 494\text{nm}$ and (c) $\lambda = 600\text{ nm}$. In Figure 18a it is observed the clear dominance of an $m = 1$ in plane dipole emitting more efficiently at the edges, and particularly, accounting a brighter emission at the edge in contact with the center of the array (top edge in the image) than at the outer one. Thus, this overall asymmetric resonance obtained probably owes to the hybridization of an $m = 1$ dipolar mode with higher order modes that shape this behavior. In Figure 18c one can observe high CL intensities at one of the edges (the edge in contact with the array again) that probably arise from the sum of an $m = 0$ resonant mode and higher order modes.

Figure 18b shows a dominant $m = 1$ dipolar resonance for one nanopillar situated at the center of the array (130 x 220 nm) at $\lambda = 488\text{ nm}$. In Figure 18d it is observed the dominance of an $m = 0$ out of plane dipolar resonance for $\lambda = 580\text{ nm}$ owing to the bright spot that arises at the center of the nanopillar.

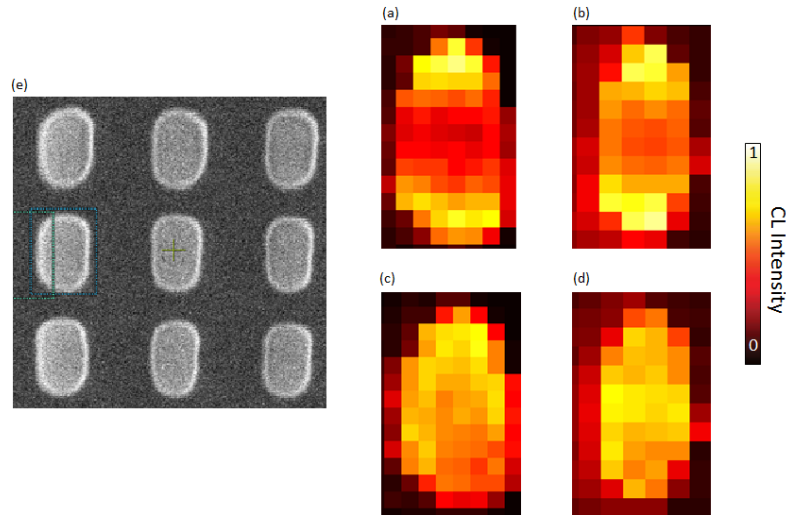


Figure 18. The first column (a and c) shows the resonances of the nanopillar situated at the vertex of the array (150 x 230 nm). (a) Dominance of an $m = 1$ dipolar resonance hybridized at $\lambda = 494$ nm. (c) Hybridized mode profile presented brighter in one edge of the nanopillar for $\lambda = 600$ nm. The second column display the resonances of one nanopillar standing out approximately at the center of the array (130 x 220 nm). (b) $m = 1$ dipolar resonance at $\lambda = 488$ nm. (d) $m = 0$ out-of-plane dipole at $\lambda = 580$ nm. (e) SEM Image of the nanopillar's array.

Therefore, it has been observed in the CL intensity maps asymmetric profiles of resonances emitting brighter always at the same edge for the nanopillar at the vertex whereas the centered nanopillar presents symmetric resonances that resemble the common $m = 0$ and $m = 1$ mode excitations. It then remarks that the nanopillars account different resonances depending on its position in the array and thus, it is an evidence that there are couplings within the array. The slight wavelength shift observed when comparing the $m = 1$ resonant modes regarding the vertex and centered nanopillar (Figure 18 (a, b)) probably owes to size differences between them and not the couplings in the array. This phenomenon is well known and it has been explained in previous analyses.

4.2. Gold/Silicon nanostructures

The CL images obtained for the Si nanostructures recovered by an Au layer present high resolutions accounting pixel sizes of 12 nm on average. The main reason that explains this huge change in resolution owes to Au is an excellent conductor, thus the transport

of electrons in the nanostructure is relatively fast and efficient. Moreover, we have attached two copper thin layers on the sample to further increase the conductivity in the CL analyses.

In relation to the Au/Si nanostructures, we expect to find a coexistence of hybridized modes accounting different natures as the electrons can travel along the Au surface of the nanostructures (generating SPPs and TR emission) or they can be trapped within the Si nanostructures expecting therefore Mie resonances and Mie optical resonant eigenmodes.

4.2.1. "Isolated" nanorods

In the next chapter, we present and discuss both the CL spectroscopy and COMSOL simulated results regarding four Au covered Si nanorods in an Au/Si substrate accounting different diameters (309, 329, 404, 520 nm) and a homogenous height (240 nm).

We have used the CL spectroscopy for the Au/Si nanorods setting 546 pA of intensity current, a pixel size of 10 nm on average and an exposure time per pixel of 1 s. The CL intensity maps observed in Figure 20 have been averaged over a 20nm-bandwidth. We will use again the analytical model extracted from published data [25] to explain the nature of the modes that arise in the CL intensity maps agreeing with the obtained CL intensity spectra as the analytical photonic wavefunctions and their hybridizations match quite well with the resonant modes encountered experimentally.

Figure 19 (a, c) shows the CL intensity spectra for all the nanorods analyzed averaged (a) over the whole sample and (c) over the centered pixels. The whole averaged CL intensity spectra, (a), present a huge overlapping of resonant peaks and thus, a broad overall band that seems to red-shift when the diameter increases. In contrast, the center averaged CL intensity spectra obtained in (c) show clearly the resonant peaks that emit light more efficiently at the center of the nanorod (they are more enhanced, it results from the center averaging). It is observed a main resonant peak that red-shifts for increasing diameters going from a peak wavelength of $\lambda = 670$ nm for the 309 nm-diameter nanorod ((c), dark blue line), a peak wavelength of $\lambda = 690$ nm for the 329 nm-diameter ((c), light blue line) to a peak wavelength of $\lambda = 750$ nm for the 404 nm-

diameter one ((c), yellow line). Comparing the resonant wavelength peaks with their respective CL maps, we find a strong agreement observed in Figure 20 (n-q), where the same hybridization of modes, the $\{m = 0, q = 2\}$ and the $\{2, 1\}$, arise in the different nanorods for sweeping wavelengths of (n) $\lambda = 670$ nm, (o) $\lambda = 690$ nm, (p) $\lambda = 750$ nm and (q) $\lambda = 810$ nm as expected.

The fact that resonances progressively red-shift and broaden when the size of the particle increases owes to retardations of the depolarization field across the nanoparticle and radiating damping terms, according to the literature [27].

Figure 19 (b, d) shows the simulations obtained from the COMSOL model proposed for the Au/Si “isolated” nanorods in an Au/Si substrate that represent the normalized outflow power in function of the wavelength, (b) averaging over all the sweep points calculated and (d) taking the centered position of the nanorod. We can observe that the simulated spectra present wavelength resonant peaks considerably red-shifted with respect to the experimental data. In (b), the broad bands are practically identical for all the nanorods, pointing at the huge overlapping between modes when considering all the surface, and the wavelengths accounting the peaks of the broad bands are shifted as well with respect to the ones obtained experimentally. In (d) we can observe similar patterns regarding the shapes of the resonant peaks between the numerical and experimental results, though the resonant peaks appear more enhanced and red-shifted in the simulated data. For example, the main peak observed in the CL spectrum for the 309 nm-diameter nanorod at $\lambda = 670$ nm, in the simulated results it seems to appear more intense, sharper and shifted at $\lambda = 790$ nm. Moreover, the small resonant peak shown for $\lambda = 500$ nm in the CL spectrum, appears strongly enhanced and red-shifted as well in the simulations at $\lambda = 560$ nm.

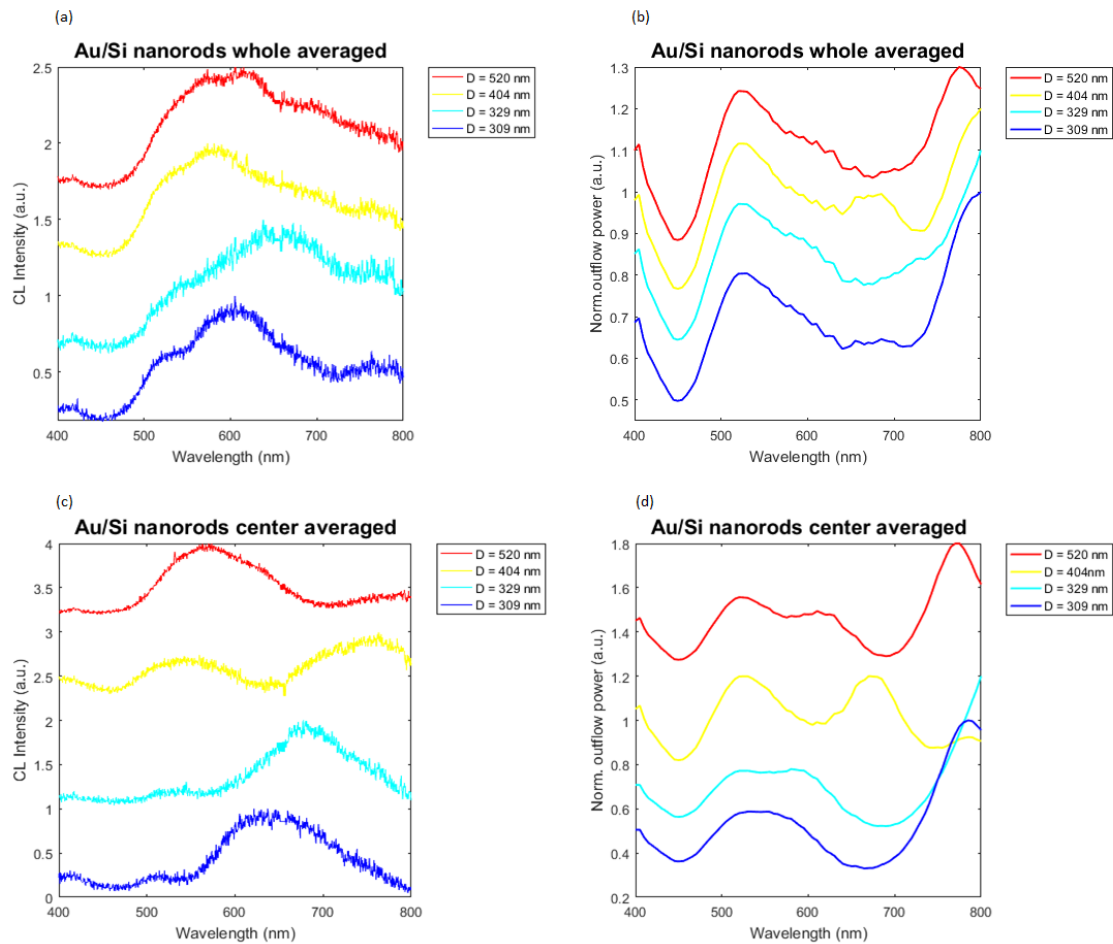


Figure 19. CL Intensity spectra and COMSOL simulations obtained for 4 Au/Si nanorods accounting different diameters (309, 329, 404, 520 nm). (a, c) Normalized CL intensity spectra in function of the wavelength averaged over (a) all the surface, (c) a handful of pixels at the center. The y axis has been cut off for clarity. (b, d) COMSOL-simulated normalized outflow power spectra (b) averaged over all the sweep points calculated and (d) taken just at the center of the nanorods. (a) High overlapping between modes and similar, slight red-shifted broad bands obtained for all the nanorods. (b) The resultant resonant peaks are quite sharper and shifted with respect to the experimental ones. (c) Clear resonant peaks observed, for increasing diameters they red-shift in wavelength and higher order modes appear. (d) The simulations show a considerable red-shift and more enhanced resonant peaks with respect to the experimental obtained ones.

Figure 20 shows a detailed scheme accounting all the resonant modes that arise for the different nanorods analyzed in the visible range of wavelengths. Each column shows the resonant modes of a nanorod at different wavelengths. Thus, from left to right columns the diameter-nanorods are: 309, 329, 404 and 520 nm, respectively. Moreover, for the

sake of clarity, each row in Figure 20 presumably presents the same resonant modes (arising at different wavelengths) for the different nanorods. It could also constitute a clear evidence that the wavelength peaks of the resonant modes red-shift when the diameter increases. It can be noticed that for some CL maps the hybridization of resonant modes is difficult to see, therefore the consistency that the analytical model from published data presents will help us to explain and clarify some of the higher order hybridizations encountered.

In Figure 20a it is presented a SEM image of a large Si nanorod, we can observe that the edges are brighter and, thus, the limits of the nanorod are not completely clear. Figure 20 (b-c) shows presumably a hybridization of an $\{1, 3\}$ higher order dipolar mode and a $\{3, 2\}$ higher order octupolar mode for $\lambda = 470$ nm and $\lambda = 530$ nm. These resonant modes are characterized to radiate inefficiently at the center, in contrast to what it is observed in the CL maps in (b) and (c) where a centered radiation can be observed. It owes to the third order dipolar resonant mode that arises present two bright spots very close to the center, thus, even the right center is not expected to be excited, the images show an overall centered brightness spot.

In Figure 20 (d-e) it is observed a dominant $\{0, 3\}$ out of plane high order dipolar resonance for $\lambda = 570$ nm and $\lambda = 625$ nm, respectively, matching perfectly with respect to the correspondent photonic wavefunction obtained in the analytical model (see Figure 12). The resonant mode is possibly hybridized with a $\{2, 2\}$ quadrupolar resonance but it is not clear. Figure 20 (f-i) shows a single resonant high order mode that arises in all the nanorods studied within the visible wavelength for $\lambda = 550, 575, 630$ and 685 nm, respectively. It is presumably the $\{2, 2\}$ quadrupolar resonance, which presents an inner bright ring that is the sum of four symmetric spots. The CL maps referring to the shorter nanorods (f, g) do present a high uncertainty and asymmetry in the resonances. Annex I gives one reasonable explanation for these anomalies observed.

In Figure 20 (j-m) it is presented the dominant hybridization of the $\{1, 2\}$ dipolar high order resonant mode and the $\{3, 1\}$ octupolar mode for $\lambda = 600, 625, 680$ and 730 nm, respectively. In (l) and (m) it can be noticed the two symmetric spots appearing concentrically near the center. Again, the CL intensity maps regarding the shortest nanorods, (j, k), do not present clear resonant emission modes. Figure 20 (n-q)

presumably shows the dominance of the hybridized $\{2, 1\}$ quadrupolar mode and $\{1, 1\}$ in plane dipolar resonant mode that appear in all the nanorods analyzed for $\lambda = 670, 690, 750$ and 810 nm, respectively. In relation to the larger nanorod, these hybridized resonant modes seem to have its peak of intensity for wavelengths rounding the 900 nm, thus, at $\lambda = 810$ nm we can observe just the starting of this mode. And finally, we can observe in Figure 20 (r-s) the primitive $m = 1$ ($\{1, 1\}$) in plane dipolar resonant mode for $\lambda = 780$ nm and $\lambda = 800$ nm in the shortest nanorods ($D = 309, 329$ nm).

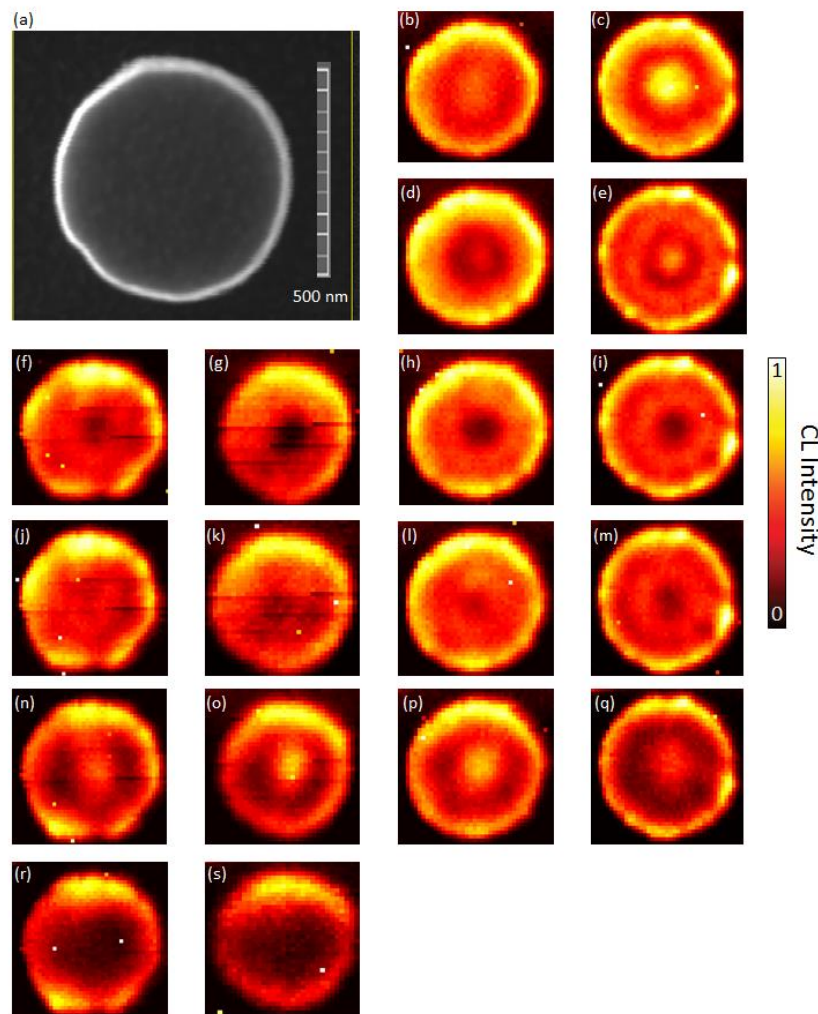


Figure 20. CL normalized emission maps for Au covered Si nanorods integrated over a 20 nm-bandwidth. From left to right column the nanorods displayed have respectively the next diameters: $D = 309, 329, 404, 520$ nm. (a) SEM image of a nanorod. (b-c) Hybridization of $\{m = 1, q = 3\}$ and $\{3, 2\}$ higher-order modes presented for the largest nanorods at (b) $\lambda = 470$ nm and (c) $\lambda = 530$ nm. (d-e) Dominance of the hybridized modes $\{0, 3\}$ and $\{2, 2\}$ for the largest nanorods at (d) $\lambda = 570$ nm and (e) $\lambda = 625$ nm. (f-i) Appearance of a single resonant mode, $\{2, 2\}$, in all the nanorods studied for (f) $\lambda = 550$ nm, (g) $\lambda = 575$ nm, (h) $\lambda = 630$ nm and (i) $\lambda = 685$

nm. (j-m) Hybridization of {1, 2} and {3, 1} resonant modes for (j) $\lambda = 600$ nm, (k) $\lambda = 625$ nm, (l) $\lambda = 680$ nm and (m) $\lambda = 730$ nm. Dominance of the hybridized {0, 2} and {2, 1} resonant modes for (n) $\lambda = 670$ nm, (o) $\lambda = 690$ nm, (p) $\lambda = 750$ nm and (q) $\lambda = 810$ nm. (r-s) $m = 1$ in plane primitive dipolar resonance ({1, 1}) found for the shortest nanorods at (r) $\lambda = 780$ nm and (s) $\lambda = 800$ nm.

Interestingly, the hybridized resonant modes identified in the Au covered Si nanorods by means of the analytical model extracted from published data match quite well with the ones presumably identified for the Si nanorods in the visible wavelength. The resonant peaks presented for the Au/Si nanorods are slightly red-shifted and brighter (observed in the CL intensity maps) in comparison to the ones obtained in the Si nanorods. The quite well presumably match in the resonant modes obtained and the red-shift in wavelengths probably means that the resonances observed both in Si and Au/Si nanorods principally owe to the geometry and size of the nanoparticle rather than its composition, thus we have observed Mie-like resonances. Therefore, the 35 nm-thickness Au layer has enlarged the particles generating a red-shift in the peak wavelengths but it is not clear that SPPs have arisen on the Au surface as we do not count with any evidence of it. The Au layer (35 nm) should not change hugely the electric field generated within the nanorod owing to its small thickness, but this thickness is large enough to expect SPPs.

One of the possibilities proposed arise from the theory, which states that the semiconductor incoherent resonances are more efficient than the SPPs and the overlapping between them in the visible range does not allow to see the coherent SPPs resonances properly. The enhanced brightness observed in the Au/Si nanorods owe to the good Au conductive properties.

Moreover, if the SPPs were observable, we could expect a reduction in the visibility of the resonance modes as the size of the Au/Si nanoparticles increase regarding its rising SPP propagation losses [13] in the Au layer. This phenomenon does not seem to arise along the CL measurements presented for the Au/Si nanostructures.

The mismatching observed between the experimental and simulated results regarding the spectra in function of wavelength for the Au/Si nanorods probably owes to an incorrect consideration of the Au thickness layer deposition in the lateral surface of the

nanorods in the settings of the model. The sputtering technique was supposed to recover the Si sample with a 35 nm-thick Au layer (though some CL intensity maps seem to present anomalies commented in the Appendix I due to a probable irregular Au deposition) but the Au deposition in the lateral surfaces is not trivial to measure as the SEM images show blurred edges in the nanostructures, making it impossible to distinguish the limits of the nanorod with a full precision. We have considered an Au deposition at the lateral surface of 10 nm in our model, probably surpassing the real deposition thickness. This incorrect supposition in the Au lateral thickness has probably brought about the red-shift observed in the simulated resonant peaks in comparison to the experimentally obtained regarding that the resonances observed for both Si and Au/Si nanostructures principally owe to Mie-type resonances as the nanoparticle sizes are comparable to the wavelength. Another possible reason for the mismatch owes to the inhomogeneous lateral Au layer deposition along the z axis, lending a larger width in the basement of the nanorod than on the top. Further research is open in the optimization of the COMSOL model parameters considering different Au layer thicknesses and dispositions.

4.2.2. "Isolated" nanopillars

Now, the results regarding Si nanopillars covered up with the Au layer are presented. In the CL analysis, we raster scan the electron beam (546 pA intensity current) over the surface of the nanopillars taking a pixel size of 15 nm and considering an exposure time of 1s per pixel.

We can observe in the CL intensity maps (Figure 21) similar eigenmodes as the encountered for the Si nanopillars (Figure 16), but slightly red-shifted in wavelengths and more intense, specially at the edges. The modes obtained for the Au/Si nanopillars are the result of hybridizations between the possible SPPs generated in the gold's surface and the cavity resonances generated within the Si. It is not straightforward to find the pattern of variation that the Au layer recovery induces to the nanostructures, thus, it would be interesting to simulate the resonance responses of the nanostructures for different thicknesses of Au deposition, in further investigations.

In relation to the 340 x 500 nm nanopillar, a standing wave pattern is observable in Figure 21g for $\lambda = 622$ nm that refers to a 3D eigenmode with $m = 2$ through the long axis of the nanopillar and $n = 1$ in the short axis. We can note that the distance between antinodes (bright points), which is about 310 nm along the short axis, matches half the wavelength of the resonant mode presented in the nanopillar, which acts as a resonator. Figure 21j shows a $m = 1$ dipolar resonance in the direction of the long nanopillar's axis for $\lambda = 714$ nm. We note again that the distance between the two antinodes through the long axis of the nanopillar, which is of 360 nm, fits half of the resonant wavelength, being coherent with the expected behavior. The starting of bright centered spots can be observed in Figures 21 (a, d, m) for $\lambda = 465, 545$ and 804 nm, respectively. As the intensity is more efficient in the center of the nanostructures (regarding that the vertex excitations may arise because of the Au deposition), it probably means that there is a dominance of an $m = 0$ azimuthal symmetric out of plane dipolar resonance except from (d) where it is observed a hybridization between an $m = 0$ dipolar out of plane resonance and a $m = 2$ quadrupolar resonance through the long axis of the nanopillar, and the second excitation seems to be the dominant.

The 314 x 380 nm Au/Si nanopillar shows the same resonance types as the 340 x 500 nm one, but shifted to shorter wavelengths attributable to retardation effects and a decreasing in the resonator's size. Figure 21 (b, e, n) shows a bright spot in the center of the nanostructure for $\lambda = 461, 525$ and 735 nm, respectively, and (e) presents the same hybridized resonances as (d). In Figure 21h it can be observed an eigenmode resonance accounting an $m = 1$ and $n = 1$ resonances with respect to the long and short axis of the nanopillars for $\lambda = 616$ nm. It is interesting to notice that the resonant wavelengths encountered in Figure 21g and Figure 21h are quite similar (622 nm versus 616 nm) and both present an $m = 1$ resonant mode along the short axis. It owes to the short length of both nanopillars are similar (345 nm versus 314 nm).

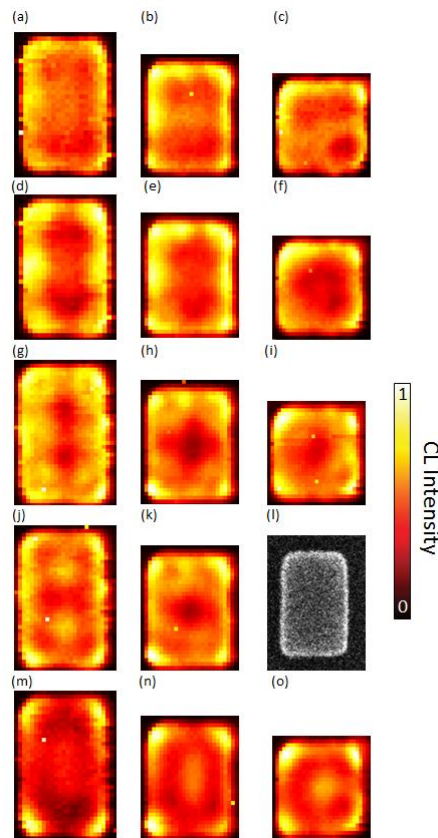


Figure 21. CL normalized emission maps for Si nanopillars covered with an Au layer 35 nm-thick. From left to right column, the sizes of the nanopillars are: 340 x 500, 314 x 380, 290 x 320 nm respectively, and the height is 300 nm with respect the substrate, homogeneous for all nanopillars. (l) SEM image of a Au/Si nanopillar. (a-o, excluding l) Two-dimensional CL intensity maps for resonant peaks. (a-f, m-o) Bright spots observed in the center of the nanostructures accounting a possible apparition of an $m = 0$ dipole out of plane resonance for $\lambda = 465, 461, 410, 545, 525, 505, 804, 735, 685$ nm, respectively. The third row (g-i) presumably presents a $n = 1$ dipolar mode along the short axis of the nanopillars for $\lambda = 622, 616, 610$ nm, respectively. In (j) and (k) it is observed a $m = 1$ dipolar mode along the long axis of the nanopillar for $\lambda = 714, 646$ nm, respectively.

Regarding the 290 x 320 nm nanopillar, the same bright spot in the center of the nanostructure is encountered in Figure 21 (c, f, o), though in (f) it is not clearly observed in the CL maps, for blue-shifted wavelengths with respect to the other larger nanopillars at $\lambda = 410, 505$ and 685 nm. An $m = 1, n = 1$ dipolar mode is observed in Figure 21i for $\lambda = 610$ nm.

To observe quantitatively the wavelength red-shifts for an increasing size of the nanopillars, it is represented in Figure 22 the center averaged CL intensity spectra

obtained for the 3 nanopillars studied. We have averaged the spectra over the center points to see again the resonant peaks accounting the bright center spots and to avoid the overlapping of other resonances.

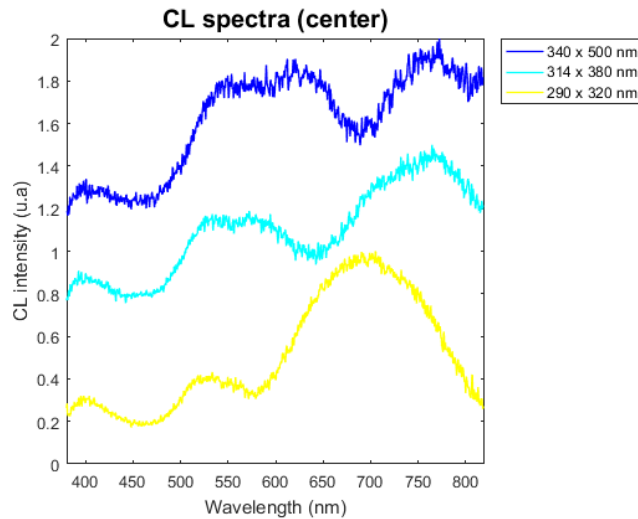


Figure 22. Spatially centered integrated CL intensity spectra for different nanopillar sizes. The normalized spectra have been vertically offset for the sake of clarity. The dominant resonance peaks show a clear red-shift for larger nanopillars.

4.2.3. “Non-Isolated” nanopillars

An array of Au/Si nanopillars with a close distance between them (50 nm in the x axis and 150 nm along the y axis) accounting an average size of 250 x 175 nm (with variations of ± 20 nm between nanostructures) and a homogeneous height of 300 nm is analyzed by means of CL and Optical spectroscopies.

It can be clearly observed in Figure 23a Fano resonance arising for wavelengths around $\lambda = 640$ nm that probably owes to an interference between a dominant and broad $m = 1$ radiative dipolar mode, shown in Figure 26c, and an antibonding feature or dark scattering state [6, 28]. It is known from the literature [15] that plasmonic materials, such as Au, show a coexistence of both broad and narrow resonances over a certain range of relative permittivities (ϵ). Though, it is not completely clear if the Fano resonance arises owing to the Si core or the Au shell of the nanostructures.

The peak intensities and wavelength positions encountered in the reflectance spectra, obtained by means of the visible spectroscopy, can change moderately when the incident angle of the polarized light varies as it is observed in Figure 23 (a, b). This phenomenon agrees with the theory already explained in the Optical spectroscopy setup section. Referring to Figure 23a, the p-polarized light impinged at 60 degrees with respect the normal axis of the sample can excite more efficiently the in-plane dipole

resonances than the one directed at 30 degrees for geometry reasons and, thus, it is observed that the reflectance intensity peaks are more defined and sharper for the 60 degrees impingement.

In relation to the s-polarized light, it is shown in Figure 23b that the Fano resonance is not excited, probably owing to an orientation mismatch between the electric polarized field and the anti-resonant feature. However, it is observed a broad resonant mode (the dips observed in the total reflectance percentage spectrum point to a resonance) for $\lambda = 575$ nm that is nothing but the $m = 1$ in plane dipolar resonance.

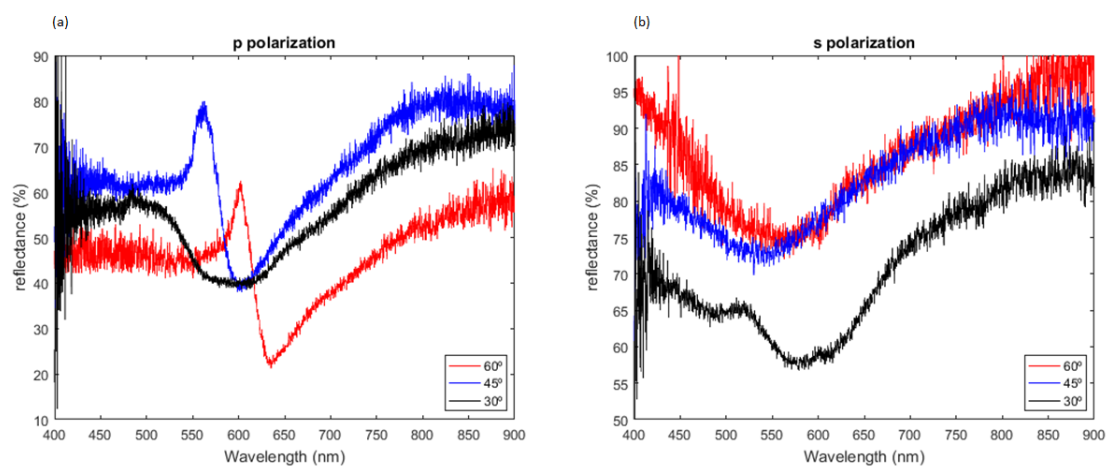


Figure 23. Optical Spectroscopy measurements taken from the ‘non-isolated’ nanopillars region impinging with a light whose angles of incidence are 30, 45 and 60 degrees with respect to the normal axis. It is represented the reflectance percentage of light in function of the wavelength. (a) P-polarized incident light, a Fano resonance can be observed in the array of nanopillars for wavelengths from $\lambda = 550$ to 650 nm. (b) S-polarized incident light, the dips observed for the three angles of incidence at wavelengths from $\lambda = 550$ to 600 nm show the $m = 1$ dipole, agreeing with the CL intensity spectrum and the CL maps obtained.

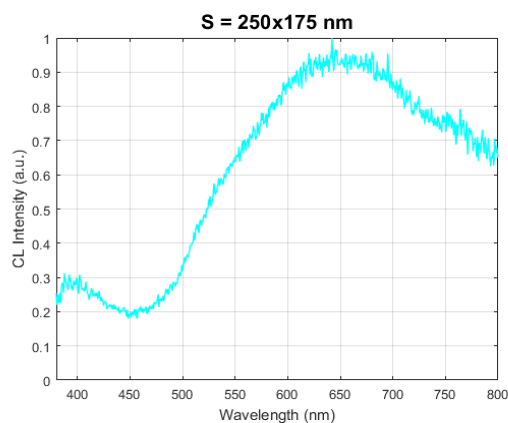


Figure 24. Spatially averaged, normalized CL intensity spectrum obtained for a nanopillar embedded in the array. It shows broad resonant peak for $\lambda = 640$ nm that agrees with the $m = 1$ dipolar resonant dominance shown in the CL intensity map (Figure 26c).

To develop the CL measurements, we use a 30 keV electron beam (546 pA intensity current) scanning 4 adjacent nanopillars in a column with a pixel size of 20 nm and 1 s of time exposure per pixel.

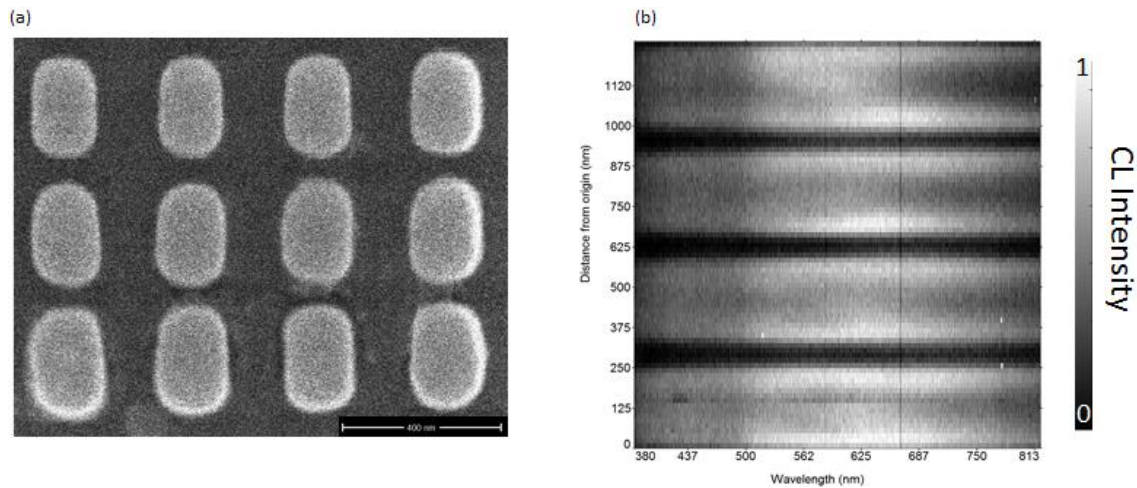


Figure 25. (a) SEM image showing a fragment of the nanopillar's array. (b) Spatially averaged CL intensity cross section taken to four nanopillars along their long axis within the whole visible range. It is observed a progressive variation in the excitation spatial spectrum over the four nanopillars for wavelengths starting from $\lambda = 625$ nm approximately.

Figure 26 shows the CL intensity maps extracted from the row of nanopillars presented at the edge of the array for wavelengths centered at $\lambda = 450$, 510 and 645 nm integrated over a bandwidth of 15 nm. The nanopillars can be clearly distinguished from the substrate as they generate large CL signals through the image.

Regarding that the nanopillars selected have approximately the same dimensions, they are supposed to present similar polarizabilities and resonant wavelengths. However, as it can be observed in Figure 26a, for $\lambda = 450$ nm, the CL emission of the nanopillars experience an increment of intensity for different nanostructures. Regarding the symmetry of the nanopillar dispositions and the intensity increments as the nanopillar is situated more in the center of the array, we can expect that this array radiates stronger in the center than in the edges. This phenomenon can be already seen, even not as clear as before, in Figure 26 (b, c) for $\lambda = 510$ and 645 nm, respectively.

In Figure 26c it can be observed for $\lambda = 645$ nm a dominance of an $m = 1$ dipolar resonance, in agreement with the Visible spectroscopy results (Figure 23), which is more accentuated for the nanopillars situated at the edges of the row. It is worth to mention

that we could not observe any resonance along the short axis of the nanopillars in the visible wavelength, probably owing to the strong overlapping of modes and the strong intensity of the dipolar resonance obtained.

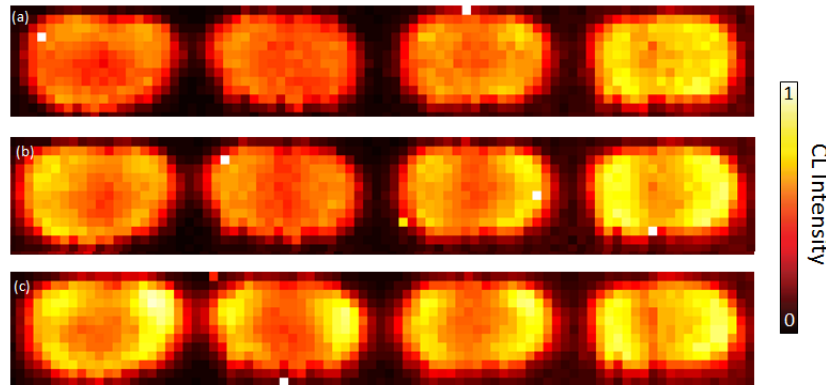


Figure 26. CL intensity maps displaying four nanopillars (175x 250 nm on average) at the edge row of the array shown in the cross section of Figure 25b for (a) $\lambda = 450$ nm, (b) $\lambda = 510$ nm and (c) $\lambda = 645$ nm detection wavelengths.

The fact that there is an increment of intensities in the nanopillars pointing supposedly towards the center of the array at certain wavelengths, as it is observed in Figure 26a, evidences the existence of couplings between nanostructures. Therefore, these resonant behaviors should be considered when the total emission generated upon local excitations is calculated.

Regarding that the Au/Si nanopillars present sizes of 175 x 250 nm on average, we are on the verge to suppose the quasi static limit, applied for nanoparticles much smaller than the wavelength. Thus, the nanopillars could be described as point dipole scatters and therefore we could assure that the $m = 1$ dipolar resonance found in Figure 26c for $\lambda = 645$ nm has an electric nature, disregarding higher-order resonances [29]. However, to be rigorous, we cannot assure that the dipolar resonance observed has an electric nature using this approximation regarding that the nanopillar's sizes are still too large. However, we know that the impinged light of the Visible spectroscopy excites predominantly electric resonances as stated in the Optical spectroscopy setup section, thus we can guess that this resonance is indeed an electric dipole.

5. Conclusions and perspectives

In this project, the optical properties of both Si and Au/Si nanostructures have been studied by means of the Cathodoluminescence spectroscopy and Visible spectroscopy (only in the Au recovered array that presented couplings) in the visible range of wavelengths. Moreover, it has been developed a model in COMSOL Multiphysics to simulate the emission spectra and the resonant peaks that arise both in Si and Au/Si nanorods by means of integrating the total outflow power regarding a vertical positioned current line that imitates the flying electrons of the CL electron beam entering the nanorod.

We have demonstrated that both Si and Au/Si nanostructures are suitable materials to be studied in the CL spectroscopy accounting a 30 keV electron beam. The resonances observed in all the nanostructures are generally the product of hybridized higher order modes. The modes observed are dominated by Mie-like optical resonances, owing to the sizes of the nanostructures are comparable to the wavelengths in the visible. Therefore, all the nanostructures studied act as resonator cavities, in agreement with the literature [6, 25].

During this project, we have confirmed many well-documented phenomena such as the red-shift of the resonant peak wavelengths when the diameters or the sizes of the nanostructures increase. What is more, we have found that Si and Au/Si materials are highly tunable materials in the visible range, sensible to changes such as the diameter, the geometry and the gratings within the array. For further research, it would be interesting to investigate the behavior tendency of the resonant modes for different Au layer thickness depositions simulating them using the model proposed in COMSOL.

To give a reasonable discretization for the different overlapped high order resonant modes observed in the Si and Au/Si nanorods, we have used an analytical model extracted from published data [25] that seems to suit and explain quite fairly the resonant modes that we have observed in the CL intensity maps. Interestingly, it has been found that the 35 nm-thickness Au recovered Si nanostructures do present similar resonant modes than the Si nanostructures (well observed in the nanopillar analyses) accounting slightly red-shifted resonant peak wavelengths. Therefore, the SPPs that

were expected to arise on the surface of the Au layer seem to be dominated by the Mie resonances within the Si cavities of the nanostructures.

Moreover, we have found coupling behaviors in both the Si and Au/Si arrays that stand nanopillars with separations about 80 and 50 nm, respectively, regarding one of the axes. In the Au/Si array we have also observed a Fano resonance which is the overlapping of a broad electric dipolar resonance and a non-radiant scattering state.

In relation to the COMSOL model proposed, it reproduces quite well the resonant wavelength peaks in the case of Si nanorods but it shows considerably red-shifted resonant peak wavelengths with respect to the experimental CL spectra obtained in the case of Au/Si nanorods. It probably owes to an incorrect supposition of the Au layer thickness in the lateral surface of the nanorods, regarding that the edges of the nanostructures appeared blurred when we used the SEM. Due to time constraints and the large simulation time consumption, we could not do more simulations sweeping over different lateral Au layer thicknesses, but it will constitute the next step to realize afterwards, considering the future publication of the results.

Further outlooks are to plot in 2D the outflow power obtained for each sweep position of the line current, regarding radial symmetry, to compare them qualitatively with the CL intensity maps obtained experimentally. A lessening in the spatial step sweep of the line current from 30 nm, which is the one considered in the project, to 5 nm will be needed to get further accurate and detailed simulated spectra and plots for the nanorods. Finally, in the future we could extend the model proposed to other geometries such as nanopillars and, afterwards, we could embed the nanostructures in periodic arrays with variable gratings in some extent to compare the simulations with the experimental CL results already obtained for the arrays with couplings.

6. Acknowledgements and conference papers

I would like to thank in the first place Prof. Anatoly Zayats for giving me the incredible opportunity to do an internship in the Plasmonics Group at King's College and Prof. Jordi Llorca for accepting to codirect my project at the distance. I am very thankful to Dr. Cillian McPolin for his guidance, his supervision and for the skills that he proportioned me in CL spectroscopy during the first months of my project. I am indebted as well to Dr. Alexey Krasavin for his assistance in COMSOL simulations and his insight in many physics-related behaviors during the simulations. I would like to thank as well to all the Plasmonics Group for their help and their kindness during all these months.

Moreover, I would like to thank Universitat Politècnica de Catalunya and King's College of London for facilitating an Academic Agreement, and the Erasmus and Agaur Scholarships for their economic support.

Finally, I would like to thank my family and my friends for their support during all my stage in London.



Figure 27. Plasmonics Group. Photo taken on March 2017.

Conference papers

Yago Nel Vila, Cillian McPolin, Alexey Krasavin, Anatoly V. Zayats, Investigation of Cathodoluminescence emission from Si and Au/Si nanostructures, *Poster at London Plasmonics Forum 2017 (London, 2017)*.

7. Bibliography

1. Moore, G.E., *Cramming more components onto integrated circuits (Reprinted from Electronics, pg 114-117, April 19, 1965)*. Proceedings of the IEEE, 1998. **86**(1): p. 82-85.
2. Curatola, G., G. Fiori, and G. Iannaccone, *Modelling and simulation challenges for nanoscale MOSFETs in the ballistic limit*. Solid-State Electronics, 2004. **48**(4): p. 581-587.
3. Anker, J.N., et al., *Biosensing with plasmonic nanosensors*. Nature Materials, 2008. **7**(6): p. 442-453.
4. Mandal, P. and S. Sharma, *Progress in plasmonic solar cell efficiency improvement: A status review*. Renewable & Sustainable Energy Reviews, 2016. **65**: p. 537-552.
5. O'Connor, D. and A.V. Zayats, *DATA STORAGE The third plasmonic revolution*. Nature Nanotechnology, 2010. **5**(7): p. 482-483.
6. Kuznetsov, A.I., et al., *Optically resonant dielectric nanostructures*. Science, 2016. **354**(6314).
7. Armani, D.K., et al., *Ultra-high-Q toroid microcavity on a chip*. Nature, 2003. **421**(6926): p. 925-928.
8. Spinelli, P., M.A. Verschuuren, and A. Polman, *Broadband omnidirectional antireflection coating based on subwavelength surface Mie resonators*. Nature Communications, 2012. **3**.
9. Brenny, B.J.M., T. Coenen, and A. Polman, *Quantifying coherent and incoherent cathodoluminescence in semiconductors and metals*. Journal of Applied Physics, 2014. **115**(24).
10. de Abajo, F.J.G., *Optical excitations in electron microscopy*. Reviews of Modern Physics, 2010. **82**(1): p. 209-275.
11. Coenen, T., *Angle-Resolved Cathodoluminescence Nanoscopy*. 2014, University of Amsterdam
12. Narvaez, A.C., et al., *Cathodoluminescence Microscopy of nanostructures on glass substrates*. Optics Express, 2013. **21**(24): p. 29968-29978.

13. Barnes, W.L., A. Dereux, and T.W. Ebbesen, *Surface plasmon subwavelength optics*. Nature, 2003. **424**(6950): p. 824-830.
14. Coenen, T., et al., *Directional emission from a single plasmonic scatterer*. Nature Communications, 2014. **5**.
15. Luk'yanchuk, B., et al., *The Fano resonance in plasmonic nanostructures and metamaterials*. Nature Materials, 2010. **9**(9): p. 707-715.
16. Yacobi, B.G. and D.B. Holt, *Cathodoluminescence Scanning Electron-Microscopy of Semiconductors*. Journal of Applied Physics, 1986. **59**(4): p. R1-R24.
17. Schubert, E.F., *Light-emitting diodes*. 2nd ed. 2006, Cambridge, UK ; New York: Cambridge University Press. x, 422 p.
18. Wang, Z.Y., et al., *Broadband optical absorption by tunable Mie resonances in silicon nanocone arrays*. Scientific Reports, 2015. **5**.
19. van de Groep, J., et al., *Direct imaging of hybridized eigenmodes in coupled silicon nanoparticles*. Optica, 2016. **3**(1): p. 93-99.
20. Coenen, T., et al., *Cathodoluminescence microscopy: Optical imaging and spectroscopy with deep-subwavelength resolution (vol 40, pg 359, 2015)*. Mrs Bulletin, 2015. **40**(5): p. 384-384.
21. Coenen, T., E.J.R. Vesseur, and A. Polman, *Angle-resolved cathodoluminescence spectroscopy*. Applied Physics Letters, 2011. **99**(14).
22. Barchiesi, D., et al., *Localized surface plasmon resonance in arrays of nano-gold cylinders: inverse problem and propagation of uncertainties*. Optics Express, 2013. **21**(2): p. 2245-2262.
23. Pierce, D.T. and W.E. Spicer, *Electronic-Structure of Amorphous Si from Photoemission and Optical Studies*. Physical Review B, 1972. **5**(8): p. 3017-&.
24. Johnson, P.B. and R.W. Christy, *Optical Constants of Noble Metals*. Physical Review B, 1972. **6**(12): p. 4370-4379.
25. Coenen, T., J. van de Groep, and A. Polman, *Resonant Modes of Single Silicon Nanocavities Excited by Electron Irradiation*. Acs Nano, 2013. **7**(2): p. 1689-1698.
26. Bohren, C.F. and D.R. Huffman, *Absorption and scattering of light by small particles*. 1983, New York: Wiley. xiv, 350 p.

27. Meier, M. and A. Wokaun, *Enhanced Fields on Large Metal Particles - Dynamic Depolarization*. Optics Letters, 1983. **8**(11): p. 581-583.
28. Zhang, J.J. and A. Zayats, *Multiple Fano resonances in single-layer nonconcentric core-shell nanostructures*. Optics Express, 2013. **21**(7): p. 8426-8436.
29. Vesseur, E.J.R. and A. Polman, *Plasmonic Whispering Gallery Cavities As Optical Nanoantennas*. Nano Letters, 2011. **11**(12): p. 5524-5530.



The work described in this project was performed at the King's College of London.